Bull Math Biol (2012) 74:2272–2314
DOI 10.1007/s11538-012-9754-9

ORIGINAL ARTICLE

A Hybrid Discrete-Continuum Mathematical Model of Pattern Prediction in the Developing Retinal Vasculature

S.R. McDougall · M.G. Watson · A.H. Devlin ·
C.A. Mitchell · M.A.J. Chaplain

Received: 5 March 2012 / Accepted: 3 July 2012 / Published online: 25 July 2012

Abstract Pathological angiogenesis has been extensively explored by the mathematical modelling community over the past few decades, specifically in the contexts of tumour-induced vascularisation and wound healing. However, there have been relatively few attempts to model angiogenesis associated with normal development, despite the availability of animal models with experimentally accessible and highly ordered vascular topologies: for example, growth and development of the vascular plexus layers in the murine retina. The current study aims to address this issue through the development of a hybrid discrete-continuum mathematical model of the developing retinal vasculature in neonatal mice that is closely coupled with an ongoing experimental programme. The model of the functional vasculature is informed by a range of morphological and molecular data obtained over a period of several days, from 6 days prior to birth to approximately 8 days after birth.

The spatio-temporal formation of the superficial retinal vascular plexus (RVP) in wild-type mice occurs in a well-defined sequence. Prior to birth, astrocytes migrate from the optic nerve over the surface of the inner retina in response to a chemotactic gradient of PDGF-A, formed at an earlier stage by migrating retinal ganglion cells (RGCs). Astrocytes express a variety of chemotactic and haptotactic proteins, including VEGF and fibronectin (respectively), which subsequently induce endothelial cell sprouting and modulate growth of the RVP. The developing RVP is not an inert structure; however, the vascular bed adapts and remodels in response to a wide variety

S.R. McDougall · M.G. Watson (✉)
Institute of Petroleum Engineering, Heriot-Watt University, Edinburgh EH14 4AS, Scotland, UK
e-mail: michael.watson@pet.hw.ac.uk

A.H. Devlin · C.A. Mitchell
Biomedical Sciences Research Institute, University of Ulster, Coleraine BT52 1SA, Northern Ireland, UK

M.A.J. Chaplain
Division of Mathematics, University of Dundee, Dundee DD1 4HN, Scotland, UK

of metabolic and biomolecular stimuli. The main focus of this investigation is to understand how these interacting cellular, molecular, and metabolic cues regulate RVP growth and formation.

In an earlier one-dimensional continuum model of astrocyte and endothelial migration, we showed that the measured frontal velocities of the two cell types could be accurately reproduced by means of a system of five coupled partial differential equations (Aubert et al. in Bull. Math. Biol. 73:2430–2451, 2011). However, this approach was unable to generate spatial information and structural detail for the entire retinal surface. Building upon this earlier work, a more realistic two-dimensional hybrid PDE-discrete model is derived here that tracks the migration of individual astrocytes and endothelial tip cells towards the outer retinal boundary. Blood perfusion is included throughout plexus development and the emergent retinal architectures adapt and remodel in response to various biological factors. The resulting in silico RVP structures are compared with whole-mounted retinal vasculatures at various stages of development, and the agreement is found to be excellent. Having successfully benchmarked the model against wild-type data, the effect of transgenic over-expression of various genes is predicted, based on the ocular-specific expression of VEGF-A during murine development. These results can be used to help inform future experimental investigations of signalling pathways in ocular conditions characterised by aberrant angiogenesis.

Keywords Retinopathy · Angiogenesis

1 Introduction

Angiogenesis is the dominant process by which new blood vessels are formed, and is characterised by sprouting of endothelial cells from pre-existing vasculature, tube and loop formation and the establishment of functional flow. During embryogenesis, organ growth and wound healing, functional vascular networks are adapted to serve the metabolic requirements of the tissue, and the spatio-temporal evolution of such networks during development is a key regulator of tissue patterning and function. It is therefore important to understand the regulation of these processes by cellular and molecular cues. In addition, angiogenesis is a major area of research interest, as a number of pathophysiological sequelae, such as necrosis, inflammation and haemorrhage (which are characteristics of tumour development, arthritis and ocular diseases such as retinopathy of prematurity and diabetic retinopathy, Folkman 1995) are closely linked with uncontrolled blood vessel development, making angiogenesis a major area of clinical interest (Carmeliet and Jain 2011).

Formation of the retinal vasculature occurs primarily by angiogenesis and, in the case of the postnatal murine eye, the factors regulating superficial retinal vascular plexus (RVP) development are relatively well understood (Fruttiger 2002; Gariano 2003). Directed movement of endothelial cells (the principal cell type forming the RVP capillaries), depends upon migration of an astrocytic network over the inner retina to the periphery: a process which begins 4–5 days prior to emergence of the first angiogenic sprouts. Astrocytes in the optic nerve head express the PDGF-A receptor

(PDGFR-α), and are induced to migrate over the inner retina in response to PDGF-A produced by retinal ganglion cells (RGCs) (Mudhar et al. 1993; Fruttiger et al. 1996). We have previously shown that in C57Bl/6J mice, astrocyte migration from the optic nerve begins between embryonic (E) day E15.5 and E18.5, and by postnatal (P) day P3 an astrocytic template covers the entire inner retinal surface (Aubert et al. 2011). Over-expression of PDGF-A in transgenic mice reduces the extent of astrocyte migration in neonatal mice (Fruttiger et al. 1996; West et al. 2005) suggesting that astrocyte migration is dependent on a gradient of PDGF-A.

Astrocytic production of chemotactic and haptotactic guidance cues provides a stable scaffold for subsequent endothelial cell migration (Dorrell et al. 2002). Prior to vascularisation, poorly oxygenated astrocytes produce VEGF-A, which in turn induces EC migration and the expansion of a nascent vascular network over the inner surface of the retina. Endothelial cell sprouting from the ophthalmic vein begins around the day of birth (P0) and a dense plexus migrates over the inner surface of the retina, reaching the retinal periphery by P8. Once a perfused vascular network has formed, astrocytes gradually downregulate VEGF-A expression (West et al. 2005; Uemura et al. 2006). There are 4 recognised mammalian VEGF genes termed VEGF A-D (Ferrara et al. 2007). As a result of alternative splicing, VEGF-A mRNA is expressed as a variety of splice-variants, each with a distinct amino acid composition and varying ability to bind heparin residues in the extracellular matrix or diffuse freely (Ferrara et al. 1992; Keyt et al. 1996; Park et al. 1993; Shima et al. 1996). In this manuscript we will focus on the role of the most widely expressed human splice variant VEGF-A_{165} and its murine homolog VEGF-A_{164}, which can both bind to ECM and diffuse in the extracellular milieu. VEGF-A_{164} is widely expressed during development (Ng et al. 2001) and is the major isoform responsible for formation of the retinal RVP (Gerhardt et al. 2003; Stalmans et al. 2002). Within endothelial cells, VEGF-A signalling is largely controlled via VEGF receptor 2 (VEGFR-2/*flk-1*) through the intracellular Dll4/Notch1 signalling pathway, which creates an alternating pattern of tip and stalk cells along the leading edge of the plexus (Baron 2003; Brooker et al. 2006). Tip cells extend filopodia and direct migration in response to a gradient of VEGF, whereas stalk cells can divide to create the growing sprouts (Gerhardt 2008; Sainson et al. 2005; Sainson and Harris 2006; Williams et al. 2006). Intra-ocular injection of VEGF-A sequestering antibodies has been found to inhibit endothelial migration and delay plexus migration (Uemura et al. 2006). Moreover, removal of the VEGF gradient in the retina, via an increased expression of VEGF-A in transgenic mouse models also reduces the extent of endothelial cell migration (Gerhardt et al. 2003; Mitchell et al. 2006), and inhibition of VEGFR2 using neutralising antibodies leads to tip cell filopodial retraction (Gerhardt et al. 2003). The molecular response of tip cells at the leading edge of the developing RVP to VEGF has been modelled by Bentley et al. (2008). It is also known that fibronectin, expressed on astrocytes, acts as a haptotactic template for endothelial cell migration. Inhibition of the ability of endothelial cells to bind fibronectin, via intra-ocular injection of anti-integrin $\alpha\beta1$ antibodies, prevents endothelial cell migration (Uemura et al. 2006).

Nascent vessel segments and the tip-cells which constitute the advancing front of vascular plexuses are closely attended by perivascular mesenchymal cells, or pericytes (Gerhardt et al. 2003; Mitchell et al. 2006). Pericytes, whose recruitment to

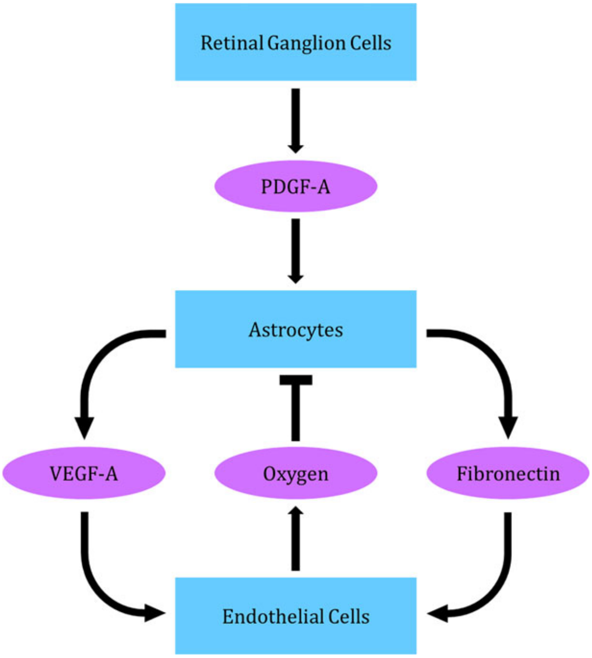

Fig. 1 Flowchart showing the key interactions between the prominent cell types involved in RVP development. Prior to birth retinal ganglion cells secrete PDGF-A, which induces astrocytes to proliferate and migrate across the inner retina. Production of VEGF-A and fibronectin by astrocytes subsequently promotes neonatal angiogenesis by endothelial cell chemotactic and haptotactic responses, respectively. Finally, the formation of blood vessels and delivery of oxygen inhibits further astrocyte activity

endothelial tubes lends functional stability to vascular networks, prevent the leakage of circulatory components and reduce the requirement of immature endothelium for survival factors such as VEGF-A. Loss of pericytes from developing or mature vasculature results in endothelial apoptosis and segment loss. Although we do not explicitly incorporate these cells into the model, their impact upon vessel pruning is taken into consideration. As the murine retina is readily accessible as a complete vascular network with 3 parallel layers, the RVP is an ideal model with which to test hypotheses on the role of endothelial cells, pericytes, matrix and chemotactic factors in generation of the functionally mature plexus. A broad summary of the mechanisms of RVP development is presented graphically in Fig. 1, highlighting the key interactions between the various biological processes.

The foregoing discussion describes an exquisitely balanced dynamic process from the field of developmental biology which provides an excellent target for mathematical modelling. Modelling of pathological angiogenesis has been extensively explored by the mathematical modelling community over the past few decades; however, there have been relatively few attempts to model angiogenesis associated with normal development. Indeed, quantitative comparisons between experimental and simulated vasculatures from well-ordered developmental processes pose a rather more rigorous test for in silico studies, as pathological vasculatures are often highly heterogeneous and consequently somewhat simpler to reproduce.

Over the past 20 years or so, mathematical modelling of vascular network development has been largely restricted to theoretical approaches that focus on the role of endothelial cells in tumour-induced angiogenesis, leading to the formation of chaotic, leaky and disorganised vascular plexuses. These models have considered a number of important mechanisms: endothelial cell proliferation, cell migration in response to different signalling cues arising from a number of soluble and diffusible angiogenic factors (chemotaxis), and haptotactic responses to insoluble molecules, such as fibronectin, present in the extracellular matrix. Most of these interactions have been modelled using systems of nonlinear partial differential equations (PDEs) that describe the migration of capillaries from a parent vessel towards the solid tumour (Anderson and Chaplain 1998; Olsen et al. 1997; Orme and Chaplain 1997; Chaplain and Stuart 1993; Byrne and Chaplain 1995; Chaplain 2000; Jackson and Zheng 2010). Some of these models have been extended to include a discrete element and used to model the progress of individual endothelial tip-cells, allowing the formation of individual capillaries to be tracked in space and time (Anderson and Chaplain 1998; Levine et al. 2001; Plank and Sleeman 2004; Stokes and Lauffenburger 1991; Bauer et al. 2007; Das et al. 2010; Anderson 2005; Owen et al. 2009a; Pons-Salort et al. 2012; Wu et al. 2008, 2009; Zheng et al. 2005). Comprehensive overviews of the modelling performed in this area can be found in the review papers of Mantzaris et al. (2004) and Peirce (2008). In contrast, blood flow modelling in a tumour-induced (micro) capillary network has only been considered relatively recently (McDougall et al. 2002, 2006; Alarcon et al. 2006; Stephanou et al. 2005, 2006; Szczerba and Szekely 2005; Szczerba et al. 2009). A review of the mathematical modelling of perfused angiogenesis can be found in Chaplain et al. (2006), which discusses the development of adaptive dynamic networks (i.e. networks that evolve both spatially and temporally in response to their associated flow distribution) induced by solid tumour growth. Models that couple perfused angiogenesis to the growth of the tumour itself include those reported by Macklin et al. (2009), Owen et al. (2009b), Welter et al. (2008, 2009), Shirinifard et al. (2009), Cai et al. (2011) and Perfahl et al. (2011).

A second important application of angiogenesis modelling concerns the healing of wounds, and in particular dermal wounds. However, although there has been a number of continuum PDE approaches applied in this context (Schugart et al. 2008; Xue et al. 2009; Pettet et al. 1996; Flegg et al. 2009), there have been few attempts to include discrete aspects of the angiogenic response to injury (Machado et al. 2010). The main focus of attention in such models has been the prediction of oxygen tension within the wound domain and several studies have attempted to approximate this by assuming a direct correlation between oxygen tension and an averaged capillary density. However, the ability of blood to deliver oxygen to regions of hypoxic tissue is very much dependent upon the *architecture* of the developing neo-vasculature and the distribution of oxygen-carrying erythrocytes (red blood cells, RBCs) within it. Hence, ideally some sense of bed topology should be considered when attempting to model wound oxygenation levels and the corresponding healing outcomes. Bed architecture is highly dependent upon a number of flow-mediated stimuli and previous models of perfused angiogenic responses have tended to over-simplify these mechanisms—aspects such as plasma skimming, phase separation, and metabolite convection have been approximated rather broadly (McDougall et al. 2002, 2006; Alarcon et al. 2003, 2006; Stephanou et al. 2005, 2006; Macklin et al. 2009; Owen et al. 2009b; Welter et al. 2009). The work described in this paper seeks to incorporate these critical aspects of blood flow in a far more rigorous manner than has previously been considered. Indeed, it will be shown that modelling the development of retinal vasculature represents a major challenge to the angiogenesis models of the past, and that progress can only be made through the inclusion of the latest developments in vascular research.

The growth and differentiation of the mammalian neural retina occurs postnatally in a highly reproducible and spatiotemporally distinct manner, providing an excellent in vivo model system. Retinal vascular plexus (RVP) formation is dependent on the establishment of a multi-layered, interlinked vascular supply. The relationship between the developing vasculature, its constituent cell types and the molecular cues that regulate this process can be easily visualised (Uemura et al. 2006). There have only been a small number of modelling studies reported in the literature concerning the growth and function of the vasculature in the eye (Jackson and Zheng 2010; Maggelakis and Savakis 1996, 1999; Liu et al. 2009). The recent work of Jackson and Zheng (2010) pertains not to the retina, but in fact models angiogenic growth in the cornea. The aim therein was to develop a hybrid model capturing the key relationships between discrete endothelial proliferation and capillary sprout extension and maturation. Maggelakis and Savakis (1996, 1999) employed a simple continuum PDE approach to investigate the interplay between VEGF, oxygen and capillary density in pathological retinal angiogenesis. Some mathematical analysis has also recently been carried out on fixed, fully developed retinal vasculatures obtained by either in vivo or ex vivo visualisation. For example, Liu et al. (2009) used a small arterial network obtained from a young, healthy adult to investigate the distribution of flow and oxygen partial pressure both across the network and within individual vessel segments. More closely related to the work in this paper, however, is the haemodynamic analysis carried out by Ganesan et al. (2010) in a full three-layer murine retinal network constructed by a combination of image-based and algorithmic approaches. We have recently developed a simplified one-dimensional continuum model of the superficial RVP, focusing on the migratory response of astrocytes and endothelial tip cells to PDGF-A and VEGF-A (Aubert et al. 2011), and to our knowledge this represents the first attempt to model vascular plexus formation in the retina during normal physiological development.

While the resolution of the simplified 1D model gives an approximate indication of the evolution of cell density and growth factor concentration profiles, a more complete hybrid PDE-discrete modelling approach is required to adequately reproduce wild-type retinae, in order to make predictions of development in the eyes of transgenic mice. The hybrid formulation allows for the tracking of individual cells, visualisation of blood vessel topology, and the dynamic remodelling and capillary pruning phenomena associated with in vivo retinal formation. In this study we focus on events during murine retinal development between embryonic day 15.5 (E15.5) and post natal day 8 (P8), by which time the superficial RVP has reached the outer perimeter of the inner retinal surface. The roles played by growth factors on cell migration—the production of VEGF-A by astrocytes and the chemotactic response of astrocytes and endothelial cells to PDGF-A and VEGF-A, respectively—are considered and blood perfusion is included throughout plexus development. The emergent retinal trees are allowed to adapt and remodel in response to various biological factors.

The in silico RVP structures generated by the model are compared with corresponding experimental sections at various stages of development, and the agreement found is highly encouraging. Having successfully benchmarked the model against wild-type data, a range of predictions on retinal angiogenesis in transgenic animals is reported to help inform future experimental investigations of signalling pathways in ocular conditions characterised by aberrant angiogenesis. It should be noted that, subsequent to P8, vertical sprouting from the superficial RVP into the deeper neural layers of the retina leads to the formation of two additional interconnected RVP layers, which are fully established by P16. The application of the model to investigate the development of these additional layers is not explicitly considered here, but will be the focus of a future publication.

2 Formation of the Murine Superficial Retinal Vascular Plexus In Vivo

Throughout this study, experimental measurements at various developmental stages, from embryonic day 15.5 to post natal day 8 (E15.5–P8) were used to inform the corresponding hybrid mathematical modelling approach, including retinal dimensions and the extent of astrocyte and endothelial cell migration. C57BL/6J mice were euthanised and, following enucleation and fixation of the globe, retinal whole mounts were prepared as previously described (Gerhardt et al. 2003). Prior to euthanasia, some animals were trans-cardially perfused under terminal anaesthesia with 150 kDa FITC-dextran (Sigma-Aldrich, UK) in order to image flowing microvascular segments at the leading edge of the expanding RVP. All animal experimental procedures conformed to UK Home Office Guidelines. Astrocyte nuclei were detected with the pan-astrocytic antibody rabbit anti-Pax2 (Covance, Leeds, UK) and endothelial cells identified using isolectin-B4 biotin-conjugate (*Griffonia simplicifolia* [GSI-B4]: Sigma, Gillingham, UK). Rabbit anti-fibronectin antibody (Sigma) was used to detect the astrocyte network. Streptavidin-conjugated or anti rabbit Alexa-Fluor 488 and 633 secondary antibodies (Invitrogen, Paisley, UK) were used as fluorophores. Images were captured using a SP5 confocal microscope (Leica Microsystems GmbH, Wetzlar, Germany) at a range of objective magnifications.

Typical retinal whole mount preparations corresponding to a series of stages in formation of the superficial RVP (from P0 to P8) are shown in Figs. 2a and 2b. Astrocyte migration and endothelial plexus migration occur in conjunction with significant retinal growth (Fig. 2c). Retinal size (measured as the distance from the centre of the optic nerve chiasm to the retinal edge) increases approximately 2-fold between E15.5 and P5 (Mean ± SEM of 975.6 ± 6.5 µm and 2189.1 ± 13.1 µm, respectively). At E15.5, Pax2 immunoreactive astrocytes are located within the border of the optic nerve chiasm. By E18.5, a dense network of Pax2 positive nuclei is observed around the optic nerve reaching halfway across the retina (Fig. 2a), and astrocytes extend to the retinal periphery at P3. Formation of the superficial RVP begins at P0, when a dense network of GSI-B4 immunoreactive endothelial cells are observed surrounding the rim of the optic nerve chiasm (Fig. 2a). The mean ± SEM number of angiogenic sprouts at P0 was quantified to be 68 ± 7 ($n = 5$). The endothelial cell plexus expands across the surface of the retina, with a distinct vessel plexus architecture established by P3, which reaches approximately halfway across the retinal surface by P5 and the periphery by P8. At P3 the superficial RVP is characterised by a dense, highly

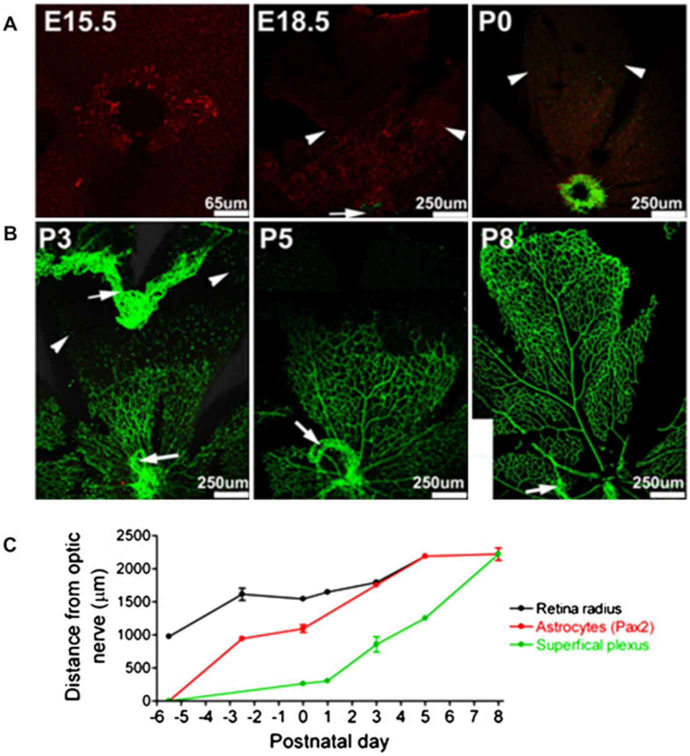

Fig. 2 Astrocyte and endothelial migration occur in parallel to retinal growth during formation of the superficial retinal vascular plexus. (**A**, **B**) Extent of astrocyte (Pax2, *red*) and endothelial cell (Iso-B4, *green*) migration in confocal images of immunohistochemically stained murine retinal wholemounts at various embryonic (E) and postnatal (P) stages (day of birth P0 = E21.5). Please note the globe-shaped retina has been cut and flattened into a petal-like shape; *arrowheads* in A indicate the extent of astrocyte migration, *arrowheads* in B indicate isolectin-B4 positive microglial cells, *arrows* in A and B indicate remnants of the embryonic hyaloid architecture which supplies the growing lens. (**C**) Quantification of retinal radius, astrocyte and endothelial migration during formation of the superficial RVP in neonatal mice. Distances are measured from the centre of the optic nerve to the furthest extent of the plexus; mean ± SEM, $n \geq 4$ at each time point

branched vessel network. Differentiated arterioles and venules are evident by P3, and by P5 a permanent pattern of five pairs of alternating arterioles and venules is established. The dense immature plexus is also "pruned" in a remodelling wave, which begins near the optic nerve chiasm around P3, and extends radially outwards as the immature RVP approaches the retinal periphery. At P5, a capillary-free zone is evident near the optic nerve chiasm, extending along arterioles; however, venules are not extensively pruned. By P8, pruning of vessels is conspicuous around primary arterioles across approximately 70 % of the retinal radius, with clear vessel free zones surrounding secondary arterioles (Fig. 2b).

Micrographs taken at higher magnification illustrate the key interactions between astrocytes and endothelial cells during RVP formation. Fibronectin immunoreactivity is not detected on the retinal surface at E15.5 prior to astrocyte migration; how-

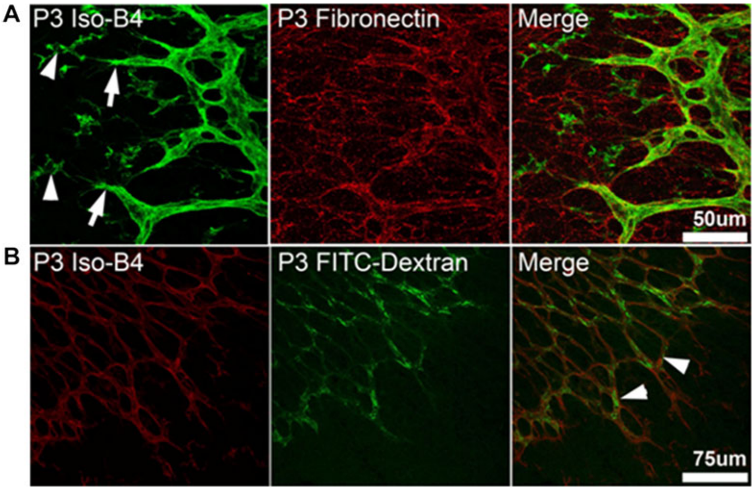

Fig. 3 Astrocytes act as a template for endothelial sprouting and formation of the perfused RVP. Immunohistochemically stained confocal images of murine retinal wholemounts at postnatal day 3 (P3). (**A**) The astrocyte network expresses fibronectin (*red*) which acts as a template for endothelial cell growth (Iso-B4, *green*). Endothelial tip cells at the leading edge of the migrating retinal vascular plexus (*arrows*) extend fine filopodial extensions over the fibronectin network. Isolectin-B4 positive microglia cells are also observed (*arrowheads*). (**B**) Co visualisation of the leading edge of the vascular plexus (Iso-B4, *red*) and fluorescent FITC-dextran (*green*); perfused migrating retinal vascular plexus (*arrowheads*) is observed up to the region immediately behind endothelial tip cells

ever, the pattern of fibronectin immunoreactivity closely matches the pattern of Pax2 immunoreactivity at both E18.5 and P3. High-power micrographs illustrate that endothelial tip-cells extend fine filopodial processes along the fibronectin networks produced by astrocytes (Fig. 3a). To investigate whether flow-mediated remodelling could play a significant role in the pruning of the plexus during the earliest stages of RVP remodelling, we determined the extent of perfusion in the plexus at P3. Perfused vessels are detected up to the leading edge of plexus formation, excluding tip-cells, indicating that the immature leading edge of the RVP contains flowing vessels (Fig. 3b).

Having discussed the cellular processes involved in RVP formation, attention now turns to the derivation of the corresponding mathematical model, which was informed by the range of morphological and molecular data obtained from several days prior to birth to approximately 8 days after birth.

3 A Mathematical Model of the Developing Retinal Vasculature

3.1 Cell Migration

In order to produce an effective mathematical model of the developing retinal vasculature, it is imperative that the approach is firmly coupled to the associated experimental programme. The model begins with the emergence of astrocytes from the optic nerve region at embryonic day 15 (E15) and follows their migration across the inner retinal surface up to post-natal day 8 (P8). The migration occurs primarily in response to a chemotactic gradient of PDGF-A (p) produced by the underlying plexus of retinal ganglion cells (RGCs; formed at an earlier stage of development and matured by day E15). Astrocytes also exhibit some degree of random motility through the extension of numerous processes and are thought to respond haptotactically to gradients of extracellular RGC-bound proteins (e). The governing dimensionless equation describing astrocyte migration can consequently be summarised as:

$$\frac{\partial a}{\partial t} = \underbrace{D_a \nabla^2 a}_{\text{diffusion}} - \underbrace{\nabla \cdot \left(\frac{\chi_p a}{(1+\xi_p p)} \nabla p \right)}_{\text{chemotaxis}} - \underbrace{\nabla \cdot (\rho_e a \nabla e)}_{\text{haptotaxis}}. \tag{1}$$

The parameters D_a, χ_p and ρ_e characterise random motility, chemotactic response to VEGF-A and haptotactic response to RGC-bound protein, respectively. Note that the chemotactic function, $\chi_p(p) = \chi_p/(1 + \xi_p p)$, where p is the concentration of PDGF-A, reflects the experimentally observed chemotactic response of astrocytes to PDGF-A gradients, namely a decreased chemotactic sensitivity at high PDGF-A concentrations. Equation (1) describes the spatial and temporal evolution of astrocyte *density*; the application to the tracking of individual astrocyte tip cells (a_i) will be described in Sect. 3.3. Full details of the non-dimensionalisation process can be found in Aubert et al. (2011). During migration, astrocytes at the leading edge of the developing front bind PDGF-A, which is also free to diffuse and decay within the retinal tissue. Therefore, the dimensionless partial differential equation characterising the evolution of PDGF-A concentration is

$$\frac{\partial p}{\partial t} = \underbrace{D_p \nabla^2 p}_{\text{diffusion}} - \underbrace{\eta_p a_i p}_{\text{uptake}} - \underbrace{\sigma_p p}_{\text{decay}}, \tag{2}$$

where D_p is the normalised PDGF-A diffusion coefficient, η_p is the uptake rate of PDGF-A by discrete astrocytes at the leading edge (a_i), and σ_p is a decay constant. Note that a_i is a Boolean value (1 or 0) that indicates the presence or absence of an astrocyte at a given position. Biologically, η_p represents binding of PDGF-A molecules to trans-membranic receptors and therefore becoming unavailable for other cells (Fruttiger 2002; Mudhar et al. 1993; West et al. 2005; Uemura et al. 2006; Gerhardt et al. 2003).

The migrating astrocytes branch in response to PDGF-A and assume a stellate phenotype, leading to the formation of a dense astrocyte mesh that forms the foundation for capillary network migration. During the formation of the astrocyte scaffold, *hypoxic* astrocytes secrete the growth factor VEGF-A (denoted c), which acts as the primary chemoattractant for endothelial cells. VEGF-A is assumed to diffuse freely through the retinal tissue; however, this is isoform-dependent (Ferrara et al. 1992; Keyt et al. 1996; Park et al. 1993; Shima et al. 1996) and will be discussed later. VEGF-A is bound by endothelial tip cells as they migrate. The dimensionless partial differential equation characterising VEGF-A activity can be written in the following form:

$$\frac{\partial c}{\partial t} = \underbrace{\alpha_c a_i^*}_{\text{production}} + \underbrace{D_c \nabla^2 c}_{\text{diffusion}} - \underbrace{\eta_c n_i c}_{\text{uptake}} - \underbrace{\sigma_c c}_{\text{decay}}, \tag{3}$$

where α_c is a measure of the production rate of VEGF-A by hypoxic astrocytes, a_i^* corresponds to the average number of hypoxic astrocytes locally, D_c is the normalised VEGF-A diffusion coefficient, η_c is the uptake rate of VEGF-A by discrete endothelial tip cells (n_i), and σ_c is a decay constant. Note that only hypoxic astrocytes produce the growth factor VEGF-A; this subtlety will become important once blood perfusion (and hence oxygen delivery) is incorporated into the model at a later stage.

Endothelial sprouts only begin to appear at the optic nerve chiasm at birth (day P0), some 6 days after the appearance of the first astrocytes; therefore, an astrocyte-induced gradient of VEGF-A exists on the retinal surface prior to endothelial migration. Endothelial cells, like their astrocyte associates, also exhibit a degree of random motility and respond chemotactically (to VEGF-A in this case) and haptotactically to gradients of matrix-bound proteins, such as fibronectin (f). The corresponding dimensionless equation describing the evolution of endothelial cell density takes a similar form to that describing astrocyte migration:

$$\frac{\partial n}{\partial t} = \underbrace{D_n \nabla^2 n}_{\text{diffusion}} - \underbrace{\nabla \cdot \left(\frac{\chi_c n}{(1+\xi_c c)} \nabla c \right)}_{\text{chemotaxis}} - \underbrace{\nabla \cdot (\rho_f n \nabla f)}_{\text{haptotaxis}}. \tag{4}$$

The parameters D_n, χ_c and ρ_f govern the random, chemotactic and haptotactic responses, respectively, while ξ_c once more quantifies reduced sensitivity to chemoattractant gradients at large concentrations. Full details of the non-dimensionalisation process can be found in Anderson and Chaplain (1998).

3.2 Matrix-Degrading Enzymes and Extracellular Proteins

The remaining equations required to complete the model of retinal angiogenesis describe the key interactions between matrix degrading enzymes and extracellular proteins, leading to the degradation of the host retinal tissue and facilitating astrocyte and endothelial cell migration via haptotaxis. Although the full molecular details of these processes in vivo are not well understood, the approach taken here has been to adopt an informed generalisation of a model previously used in the context of tumour-induced angiogenesis (Levine et al. 2001; Stephanou et al. 2006; McDougall et al. 2006; Anderson et al. 2000), whereby matrix degrading enzymes (m_a, m_n), produced by astrocyte and endothelial leading edge tip cells, respectively, reduce the local concentration of matrix-bound proteins (e, f) (Karagiannis and Popel 2006; Yana et al. 2007). To this end, astrocytes and endothelial cells at the leading edge of their respective plexuses are assumed to produce enzymes that are free to diffuse and interact with their target matrix proteins and exhibit a degree of natural decay. The matrix proteins themselves are produced locally by migrating astrocytes (Zhang et al. 2004; He et al. 2007) and are degraded by the appropriate enzyme. The corresponding dimensionless equations are

$$\frac{\partial m_a}{\partial t} = \underbrace{\alpha_{m_a} a_i}_{\text{production}} + \underbrace{D_{m_a} \nabla^2 m_a}_{\text{diffusion}} - \underbrace{\sigma_{m_a} m_a}_{\text{decay}}, \tag{5}$$

$$\frac{\partial m_n}{\partial t} = \underbrace{\alpha_{m_n} n_i}_{\text{production}} + \underbrace{D_{m_n} \nabla^2 m_n}_{\text{diffusion}} - \underbrace{\sigma_{m_n} m_n}_{\text{decay}}, \tag{6}$$

$$\frac{\partial e}{\partial t} = \underbrace{\beta_e a_i}_{\text{production}} - \underbrace{\gamma_e m_a e}_{\text{degradation}}, \tag{7}$$

$$\frac{\partial f}{\partial t} = \underbrace{\beta_f a_i}_{\text{production}} - \underbrace{\gamma_f m_n f}_{\text{degradation}}. \tag{8}$$

To reiterate: in (5) and (6), m_a and m_n represent the concentrations of matrix-degrading enzymes produced by astrocyte and endothelial tip cells, respectively. The α_i refer to the local production rates of each enzyme, D_i are the corresponding diffusion coefficients, and σ_i are decay constants. In (7) and (8), e and f refer to bound proteins (e.g. vitronectin, fibronectin), both of which are produced by astrocytes (at rates β_e and β_f) and degraded by their corresponding enzyme (at rates γ_e and γ_f). Although full details can be found in the references mentioned above (Aubert et al. 2011; Anderson and Chaplain 1998), it should be clarified here that the normalised equations (1)–(8) are obtained using a fully consistent time non-dimensionalisation. Therefore, cell densities, bound protein densities, concentrations of matrix-degrading enzymes and growth factor concentrations all evolve on an analogous timescale throughout RVP expansion.

3.3 Discrete Tip-Cell Migration and Branching

Equations (1) and (4) are continuous partial differential equations and are not in a form that can be immediately used to track individual astrocytes, endothelial cells, or discrete capillary vessels. However, such discrete entities are of primary importance here, as perfusion and vascular remodelling depend crucially upon the underlying architecture of the developing vascular plexus. In order to compare our simulations with in vivo experimental results, discretised forms of (1) and (4) are required. Following the hybrid approach outlined in Anderson and Chaplain (1998), and subsequently supported by the work of various groups (McDougall et al. 2002, 2006; Anderson 2005; Owen et al. 2009a; Pons-Salort et al. 2012; Wu et al. 2008, 2009; Zheng et al. 2005), the Euler finite difference approximation (Mitchell and Griffiths 1980) can be applied to (1) and (4). The endothelial cell or astrocyte density at a particular spatial position can subsequently be expressed as a linear combination of the densities at positions within one grid length at the previous time step, viz.:

$$n_{l,m}^{q+1} = P_0 n_{l,m}^q + P_1 n_{l+1,m}^q + P_2 n_{l-1,m}^q + P_3 n_{l,m+1}^q + P_4 n_{l,m-1}^q, \tag{9}$$

$$a_{l,m}^{q+1} = Q_0 a_{l,m}^q + Q_1 a_{l+1,m}^q + Q_2 a_{l-1,m}^q + Q_3 a_{l,m+1}^q + Q_4 a_{l,m-1}^q, \tag{10}$$

where l, m and q are positive parameters specifying either the position of the cell on the 2D grid (i.e. $x = l\Delta x$ and $y = m\Delta y$) or the current point in time (i.e. $t = q\Delta t$), and the values of the coefficients P_i and Q_i depend on the local chemical environment (i.e. matrix-bound protein and growth factor concentrations) of the astrocytes or endothelial cells, respectively. For each cell type, the appropriate coefficient values are subsequently used as directional weightings to stochastically determine the migration of an *individual* astrocyte or endothelial cell. The coefficients incorporate the effects of random movement, chemotaxis and haptotaxis, and, more specifically, are related to the likelihood of the cell remaining stationary (P_0 or Q_0), or moving to the left (P_1 or Q_1), right (P_2 or Q_2), up (P_3 or Q_3) or down (P_4 or Q_4). This approach has been used previously by the authors (and many others) in the contexts of tumour-induced angiogenesis and wound healing.

One final aspect of the cellular biology that needs to be addressed by the model is the process of astrocyte and endothelial cell branching. Migrating astrocytes are assumed to branch in response to PDGF-A, exhibiting a stellate phenotype that results in the formation of a dense astrocyte scaffold (Fruttiger et al. 1996). This experimental observation is included in a phenomenological manner through the use of branching probabilities for leading edge astrocytes that scale with increasing PDGF-A concentration (see Appendix A). Biologically, the formation of new *capillary* loops at the leading edge of the endothelial plexus is controlled by VEGF-induced filopodial extension from tip cells, via the complex intracellular Dll4/Notch1 signalling pathway, which has been modelled by Bentley et al. (2008). To approximate this in vivo observation at a discrete level, the generation of new endothelial sprouts from existing endothelial tips is again included phenomenologically, with increasing endothelial tip cell branching assumed in the presence of increasing VEGF-A concentration. The interaction of filopodia from different tip cells can ultimately lead to fusion and the formation of new capillary loops, something that is important when considering blood perfusion and vascular remodelling. Such anastamosis emerge naturally from the model when either an endothelial sprout tip cell encounters another sprout tip cell or an existing capillary at a particular location.

3.4 Blood Flow, Vessel Adaptation and Plexus Remodelling

The modelling details described in Sect. 3.3 concern cell migration in response to a number of different guidance cues, and provide an appropriate starting point for the development of an in silico model of the murine retinal vasculature. However, at this stage the model is missing a number of vital elements that depend upon the integration of blood perfusion during capillary growth. Not only does the aforementioned model for astrocyte migration (Eq. (1)) require knowledge of the evolving oxygen-laden capillary network, but the complex hierarchical in vivo structures observed experimentally can never be reproduced using simple migration equations alone, as bed organisation is profoundly influenced by perfusion-modified vessel adaptation and remodelling mechanisms.

Clearly, the ability of blood to deliver oxygen to regions of hypoxic tissue is very much dependent upon the architecture of the developing neo-vasculature and the distribution of oxygen-carrying erythrocytes (red blood cells, RBCs) within it. Moreover, since blood is a complex biphasic fluid comprising predominantly of erythrocytes and plasma, cell-cell and cell-wall interactions have a significant impact on flow distribution and vessel adaptation within a given network. Previous models of perfused angiogenic responses have tended to approximate phenomena such as plasma skimming, phase separation and metabolite convection rather broadly and some important convected and conducted stimuli have been neglected due to inherent topological complexity and computational effort. Blood vessels are capable of adapting their radii in response to various stimuli and stresses experienced during blood flow, and this adaptation introduces a feedback loop into the system, as the variation in radii will, in turn, affect the rheological properties of the blood itself. The stimuli considered in earlier papers generally follow the treatment of Pries et al. (1998), and include the effects of wall shear stress, intravascular pressure and a metabolic mechanism based on *local* flow rate. The model assumes that the radial perturbation ΔR in a flowing vessel over a time step Δt is proportional to both the total stimulus S_{tot} acting on the vessel and to its radius prior to stimulation R, accounting for the natural shrinking tendency of vessels in the absence of positive growth stimuli:

$$\Delta R = R \cdot \Delta t \cdot S_{\text{tot}} = R \cdot \Delta t \cdot (S_\tau + k_p S_p + k_{\text{metab}} S_{\text{metab}} - k_s) \tag{11}$$

where S_τ, S_p and S_{metab} correspond to stimuli associated with wall shear stress, intravascular pressure, and blood-borne metabolites, respectively. The parameters k_p and k_{metab} quantify the relative intensity of the pressure and metabolic stimuli, respectively, whilst the additional term k_s represents the shrinking tendency of a vessel: proposed to reflect the need for positive growth stimuli in maintenance of cell mass and vessel diameter (Pries et al. 1998). Further details, justification and explicit functional forms can be found in Pries et al. (1998). By coupling the endothelial cell migration equations with the flow equations, including blood rheological properties and capillary remodelling mechanisms, we can begin to simulate the response of the endothelial cells at a vascular level to the guidance cues discussed earlier and the subsequent dynamic adaptation of the flowing vascular network. However, although this approach has proved successful in reproducing reasonable vasculatures in the contexts of tumour-induced angiogenesis and wound healing (McDougall et al. 2002, 2006; Stephanou et al. 2005, 2006; Macklin et al. 2009; Owen et al. 2009b; Machado et al. 2010), it will be shown later that the retina poses a more rigorous test of any angiogenesis model and more refined perfusion mechanisms must be included to fully capture the intricacies of the in vivo observations.

Before proceeding to discuss the extension of the previous flow model to include phase separation at microvascular bifurcations and shunt-prevention mechanisms, the general method of calculating capillary flow and blood rheological properties will be restated. At the scale of a single capillary element of length L and radius R, the relationship between pressure gradient (ΔP) and flow (Q) is assumed to be Poiseuille-like;

$$Q = \frac{\pi R^4 \Delta P}{8\mu_{\text{app}}(R, H_D)L}, \quad \text{with } \mu_{\text{app}}(R, H_D) = \mu_{\text{rel}} \times \mu_{\text{plasma}}, \tag{12}$$

where μ_{app} is an apparent blood viscosity, which depends on the local blood haematocrit (H_D), vessel radius and plasma viscosity (μ_{plasma}). Accurate experimental measurement of blood viscosity in living microvessels is difficult to achieve, and so we apply the well-informed relationship derived by Pries et al. (1994):

$$\mu_{\text{rel}}(R, H_D) = \left[1 + (\mu_{0.45} - 1) f(H_D) \left(\frac{2R}{2R - 1.1}\right)^2\right] \times \left(\frac{2R}{2R - 1.1}\right)^2, \tag{13}$$

where R is the vessel radius, and $\mu_{0.45}$ and $f(H_D)$ are the viscosity corresponding to the average human haematocrit value and a function of the haematocrit, respectively. The full parameterisation of the above relationship can be found in Pries et al. (1994) or McDougall et al. (2006). Having decided upon a local flow law at the scale of an individual capillary, the next step of the modelling approach is to calculate the distribution of pressure and flow within an interconnected vascular bed. This turns out to be relatively straightforward—by conserving mass at each node of the network and using (12) and (13) to calculate the flows converging at each node, a set of linear pressure equations can be derived and solved numerically. Using these nodal pressures, the flow in each capillary element can subsequently be calculated. Whilst this approach would be wholly adequate to model pseudo single-phase flow, where the blood in each capillary is treated as a homogeneous, non-Newtonian fluid with averaged bulk properties, a more involved model is required to accurately deal with the important phenomena of axial erythrocyte migration and the formation of plasma layers.

Phase Separation Separation of plasma and red blood cells at bifurcations in the microvasculature has been widely studied both in vivo (Schmid-Schoenbein et al. 1980; Klitzman and Johnson 1982) and in vitro (Yen and Fung 1978; Fenton et al. 1985; Carr and Wickham 1991; Enden and Popel 1994). One such study conducted by Pries et al. (1989) examined the behaviour at 65 simple branch points in the rat mesentery, yielding a parametric description of phase separation in vivo

$$FQ_E = \frac{1}{1 + e^{-\{A + B\ln(\frac{FQ_B - X_0}{1-(FQ_B + X_0)})\}}}, \tag{14}$$

where FQ_B is the bulk fractional blood flow in a daughter vessel, FQ_E is the corresponding fractional erythrocyte flow in the vessel, while the parameters A, B and X_0 determine the behaviour for a particular distribution of radii and feeding vessel haematocrit. By linear regression, Pries et al. (1989) found the best fit for these parameters to be

$$A_\alpha = \frac{-6.96\ln(\frac{D_\alpha}{D_\beta})}{D_f}, \qquad B = 1 + 6.98\left(\frac{1 - H_D}{D_f}\right), \qquad X_0 = \frac{0.4}{D_f}, \tag{15}$$

where D_α, D_β, D_f are, respectively, the diameters of the two daughter branches and the feeding vessel, and H_D is the discharge haematocrit of the feeding vessel. Note the introduction of the subscript α in the first equation to denote that this is the form used to calculate FQ_E in daughter vessel α. The calculation for vessel β requires reciprocation of the D_α and D_β values, that is, $A_\alpha = -A_\beta$.

The above equations adequately describe situations where a parent vessel splits into two daughter vessels, but the *pre-pruned* vascular plexus associated with the developing retina is not so hierarchical. Consequently, the formulation must be extended to include non-uniform combinations of vessel connectivity, flow direction, parent and daughter vessel diameter, and parent vessel discharge haematocrit. A generalisation that is more widely applicable to heterogeneous vascular architectures, yet also maintains the key characteristics of the hierarchical model can be achieved through modification of the parameters in (15), viz.;

$$B = 1 + 6.98\left(\frac{1 - \langle H_{D_{\text{in}}}\rangle}{\langle D_{\text{in}}\rangle}\right), \qquad X_0 = \frac{0.4}{\langle D_{\text{in}}\rangle}, \tag{16}$$

where $\langle H_{D_{\text{in}}}\rangle$ is now the *average* discharge haematocrit over *all* parent vessels (i.e. nodal supply), and $\langle D_{\text{in}}\rangle$ is the corresponding *average* parent vessel diameter. Under the assumption of n daughter vessels we also have

$$A_i = \frac{-6.96\ln(\frac{D_i}{\langle D_{\text{out}}\rangle_i})}{\langle D_{\text{in}}\rangle}, \quad \text{with } \langle D_{\text{out}}\rangle_i = \frac{(\sum_{j=1}^{n} D_j) - D_i}{n-1}, \tag{17}$$

where A_i must be calculated for each daughter vessel downstream of the nodal supply.

Using these new parameters along with the appropriate FQ_B values, equation (14) can then be applied to determine FQ_E for each daughter vessel. This new generalised phase separation mechanism has been included in the retinal angiogenesis model and is found to have profound consequences for vascular development, haematocrit transport, and oxygen delivery to the retinal plexus.

Shunt Prevention It is clear from experimental observations (Pries et al. 1992) that a consequence of phase separation in microvascular networks is the sizeable proportion of erythrocytes in blood following the major flow pathways. Depending upon the topology of the network, this may prove highly disadvantageous with respect to oxygen delivery to the tissue, with small terminal vessels potentially receiving little or no haematocrit. In the context of tumour-induced angiogenesis, this also has major implications for chemotherapy delivery to tumours, with treatments effectively bypassing their target via dilated shunts (Stephanou et al. 2005, 2006; McDougall et al. 2006; Pries et al. 2010). In developmental biology, however, angio-adaptation in healthy tissue tends towards the prevention of large shear stresses, and so high flow shunts are relatively uncommon. Using data obtained from six rat mesenteric networks, Pries et al. (2001) modified their earlier formulation and conjectured the existence of four main stimuli that contribute to the regulation of vessel radii in the microvasculature. Two of these, the so-called “conducted” and “convected” stimuli, contribute to the prevention of shunt formation by favouring the vasodilatation of segments that are part of long flow pathways. The convected stimulus is assumed to act downstream by the addition of a metabolite to the blood, at a rate that depends on the partial pressure of oxygen (PO_2) in each segment. Conversely, the conducted stimulus acts upstream via assumed changes in electrical potential through gap junctions between smooth muscle and endothelial cells. Neither of these stimuli have been rigorously included in angiogenesis models to date.

Pries et al. (2001) proposed that the convective flux of metabolite (J_m) increases as blood perfuses downstream and that the contribution from each vessel segment of length L_s can be calculated according to

$$J_m^{\text{down}} = J_m^{\text{up}} + L_s\left(1 - \frac{PO_2}{PO_{2,\text{ref}}}\right), \tag{18}$$

whenever the intravascular PO_2 falls below the reference level ($PO_{2,\mathrm{ref}}$). Here, J_m^{down} refers to the flux of metabolite leaving a vessel segment and J_m^{up} corresponds to its upstream feeder flux. In our model, we approximate the intravascular PO_2 level by considering the volume flow of red blood cells (QH_D) in each segment. Hence, equation (18) becomes

$$J_m^{\mathrm{down}} = J_m^{\mathrm{up}} + L_s\left(1 - \frac{Q \cdot H_D}{(QH_D)_{\mathrm{ref}}}\right), \tag{19}$$

where $(QH_D)_{\mathrm{ref}}$ is a reference value for erythrocyte volume flow. Furthermore, we assume that the flowing metabolite splits in a flow-weighted fashion at diverging bifurcations. This procedure results in a value for J_m in each flowing vessel segment, which is then used to calculate the total metabolic stimulus (S_m) for local radial perturbation by the equation

$$S_m = \log\left[1 + \frac{J_m}{(Q + Q_{\mathrm{ref}})}\right], \tag{20}$$

where Q_{ref} is a small reference flow value included to prevent singular behaviour in segments with low flows.

The *conducted* response is assumed to arise in each vessel segment in proportion to the convection-derived S_m value in that segment. The signal undergoes an exponential decay, and is also split in equal proportions at diverging bifurcations. Specifically, the conducted response increases upstream, *against the flow*, and the contribution from each vessel segment is calculated according to

$$J_c^{\mathrm{up}} = \left(J_c^{\mathrm{down}} + S_m\right) \cdot \exp\left[-\frac{L_s}{L_c}\right], \tag{21}$$

where J_c^{down} and J_c^{up} are the downstream and upstream signal strengths, respectively, and L_c is the decay length constant. The total conducted stimulus (S_c) in each segment is then governed by the saturable response

$$S_c = \frac{J_c}{J_c + J_0}, \tag{22}$$

where J_0 is the saturation constant.

To complete the angio-adaptation algorithm, the conducted and convected responses are complemented by two further stimuli described by Pries et al. (2001): sensitivity to shear stress and a negative sensitivity to pressure, governed by

$$S_\tau = \log(\tau_w + \tau_{\mathrm{ref}}), \tag{23}$$

and

$$S_p = -\log\left(100 - 86 \cdot \exp\left\{-5000 \cdot \left[\log(\log P)\right]^{5.4}\right\}\right), \tag{24}$$

respectively, where τ_w and P are the segment wall shear stress and intravascular pressure, respectively. Combining these four stimuli, the rule for the radius change (ΔR) of a vessel of radius R over a time step Δt takes the form

$$\Delta R = R \cdot \Delta t \cdot S_{\mathrm{tot}} = R \cdot \Delta t \cdot \left(S_\tau + k_p S_p + k_m[S_m + k_c S_c] - k_s\right). \tag{25}$$

The additional constant k_s represents the shrinking tendency of all vessels in the absence of positive growth stimuli, while the other parameters (k_p, k_m and k_c) are introduced to allow variation of each of the individual stimuli with respect to the shear stress sensitivity. In all previous publications the method of diameter adaptation was more simplistic, and based on results from Pries et al. (1998). The metabolic stimulus widely used in previous studies,

$$S_{\mathrm{metab}} = \log\left[\left(\frac{Q_{\mathrm{metab}}}{Q \cdot H_D}\right) + 1\right], \tag{26}$$

where Q_{metab} is a reference flow rate, depends solely on *local* conditions without reference to the position of a vessel within a connected vascular bed. This has now been replaced by the modified upstream conducted and downstream convected stimuli. To reiterate, the inclusion of these refined mechanisms in earlier treatments of angiogenesis modelling has been somewhat lacking for understandable reasons; their addition has not only been computationally prohibitive in large networks but the concentration tracking algorithms required in topologically complex situations become rather involved. The new formulation *has* been included in the current model and the impact of the two new stimuli is substantial.

3.5 Oxygen Delivery and Vascular Remodelling

In the foregoing discussions of VEGF-A production by hypoxic astrocytes and metabolite release by endothelial cells, the role of local oxygen tension was highlighted as being particularly significant. Furthermore, the extent of vascular remodelling, the removal of poorly perfused vessels situated in areas of low VEGF-A concentration, is also highly oxygen dependent. In order to capture these important aspects of the angiogenic response, oxygen transport both within the vasculature itself and the host retinal tissue has been modelled.

Several previous mathematical models of tumour-induced angiogenesis have considered oxygen transport in the tumour micro-environment (Macklin et al. 2009; Welter et al. 2009; Alarcon et al. 2003). In most of these approaches, each individual capillary element is assumed to act as an oxygen source, the strength of which varies in proportion to the segment haematocrit. The main advantage of this approach is that, due to the rapid timescale of oxygen diffusion with respect to that of cell proliferation, a quasi-steady-state assumption can be invoked in the reaction-diffusion equation for oxygen. Hence, a quasi-steady oxygen profile can be calculated at each growth time step, allowing for continuous oxygen-related feedback to be considered in the migration model. However, the disadvantage of this approach is the lack of explicit coupling to the underlying capillary flow regime; the inherent assumption being that the rate of oxygen transfer across capillary walls is negligible in comparison to the rate of oxygen supply (i.e. blood flow) to each segment. This suggests that the delivery of oxygen from the vasculature to the surrounding tissues is a *diffusion*-limited process. In the microvasculature, where vessel permeability to oxygen is high and the majority of perfusion rates are relatively low, the ability to deliver oxygen depends crucially on the rate of oxygen supply and therefore the process is very much *flow*-limited (Levick 2000). In the retina, in particular, where we have a hierarchical structure of capillaries, we would expect a large degree of heterogeneity in oxygen delivery to the tissue as we move downstream from arterial to venous subregions of the plexus. During the early stages of post-natal development, the observation of differential vascular pruning in the vicinity of the arterial capillaries and the conspicuous absence of pruning around veins is believed to be a consequence of this process. In order to capture this spatial heterogeneity in the model, we must explicitly incorporate the effect of perfusion on tissue oxygen delivery. This is achieved by simultaneously solving the following coupled equations (presented here in dimensional form for ease of interpretation)

$$\frac{\partial S_T}{\partial t} = D_{ST} \cdot \nabla^2 S_T + \frac{\pi K}{2L^2} \cdot \sum_{\substack{\text{vessel}\\ \text{sources}}} \big[R_i(S_{V_i} - S_T)\big] - \sigma_{ST} S_T, \tag{27}$$

and

$$\frac{\partial S_V}{\partial t} = \frac{F Q_E}{\pi R^2 L} \cdot \sum_{\substack{\text{feeder}\\ \text{vessels}}} [Q_j S_{V_j}] - \frac{Q S_V}{\pi R^2 L} - \frac{K}{2R} \cdot \sum_{\substack{\text{tissue}\\ \text{sinks}}} [S_V - S_{T_k}], \tag{28}$$

where S_T represents the tissue oxygen concentration and S_V is the concentration of oxygen in a particular vessel. We assume that the blood-borne erythrocytes are the sole source of oxygen, carrying it into the domain from the optic nerve inlets. At any given instant, the oxygen concentration in an individual vessel segment (S_V) is assumed to be a product of the volume fraction of red blood cells in the vessel (i.e. haematocrit) and the amount of oxygen carried by those cells.

Equations (27) and (28) effectively combine three different modes of oxygen transport. Firstly, diffusion in the extracellular retinal tissue as characterised by the diffusion coefficient D_{ST} in (27); secondly, downstream convection in the vasculature as described by the first two terms in (28), where R, L and Q represent the radius, length and volume flow rate, respectively, of the segment in question; and the third mode of oxygen transport is via the transmural transfer between the tissue and the vessels, the rate of which is governed by the surface area of the vessel wall and its permeability, K. Note the appearance of FQ_E in (28), defined earlier in the phase separation description in Sect. 3.4. This defines the fraction of red blood cells at the feeding node that will enter the vessel, and is included in (28) to ensure that oxygen is distributed in the same proportion as red blood cells at bifurcations. The first term sums the contribution from each vessel flowing into the feeding node and from this the second term subtracts the concentration lost from the vessel due to the outflow at the downstream end of the vessel. Each 3D tissue element occupies the void between potential vessel positions, such that the dimensional length of each vertex is equal to the vessel segment length. Therefore the transmural oxygen transfer component in the tissue equation (27) is made up from contributions from up to 12 separate perimeter vessels. In the finite differencing scheme used here, each individual vessel shares a boundary with up to 4 neighbouring tissue blocks with an equal surface area for oxygen transfer in each, which explains the final summation term in (28). We have one final term in (27), representing removal of oxygen from the tissue at a rate σ_{ST}. This represents an effective sink term that describes not just the decay of oxygen, but also its uptake by the underlying host tissue and cellular plexuses. Throughout the period of retinal development that we consider (i.e. up to 8 days post-birth), oxygen-rich regions of the RVP contain a dense mesh of endothelial cells and astrocytes. It therefore seems reasonable to assume that the background consumption of oxygen will experience no notable spatial or temporal variations. The spatial distribution of oxygen and haematocrit throughout the retinal plexus and associated vasculature can be calculated at any given time, and these data can be used to inform VEGF-A production (through (3)), metabolite release and conducted stimulus flux (through (18), (20) and (21)), and capillary remodelling. Three conditions must be satisfied simultaneously at a vessel segment in order for pruning to occur at that location:

1. The average oxygen concentration in the tissue surrounding the vessel must be above a critical value, $S_{T\text{crit}}$.
2. The age of the vessel must exceed a critical threshold, A_{crit}.
3. The vessel must be devoid of positive flow-related stimuli (cf. (25)).

The first condition relates to the biological observation that oxygen downregulates production of VEGF, itself believed to be an endothelial cell survival factor (West et al. 2005; Scott et al. 2010; Weidemann et al. 2010). The critical age condition captures the experimentally observed lack of vascular pruning at the leading edge of the progressing endothelial plexus, which can be seen in Fig. 2b, where capillary-free zones predominantly appear behind the leading edge during the first 8 days post-birth. The final condition captures the notion that each of the flow-related stimuli have a role in providing survival signals to the vessels. In essence, this is invoked when the radius of a vessel segment has dropped to its minimum possible value (R_{min}), implying that the positive growth stimuli have failed to overcome the natural shrinking tendency (parameterised by k_s in (25)). Full mount plots of oxygen tension and capillary pruning corresponding to a number of different angiogenesis scenarios will be presented in Sect. 4.

3.6 Boundary and Initial Conditions

The largest domain considered for the computational simulations corresponds to a 4.4 × 4.4 mm retinal surface, which correlates with the maximum murine retinal diameter observed experimentally up to post-natal day 20 (P20). The underlying capillary network template consists of 220 × 220 nodes (amounting to approximately 50,000 individual capillary elements and distorted to ameliorate topological flow bias, McDougall et al. 2002). The ophthalmic vein, from which the vascular network emerges, is located at the optic nerve head, which itself sits within the optic nerve chiasm of approximately 520 μm in diameter. This is represented in the model as an equivalent tissue-free void in the centre of the numerical domain. The astrocyte network, capillary network, growth factors, matrix-degrading enzymes and bound proteins remain confined to the retinal surface, which means that no-flux boundary conditions are imposed on the inner and outer domain boundaries. In order to initiate the development of the astrocyte and endothelial plexuses, 40 astrocyte sprouts and 10 endothelial sprouts are evenly distributed around the perimeter of the optic nerve chiasm (Fig. 4). The endothelial sprouts are phenotypically labelled a priori as being either arterial or venous in

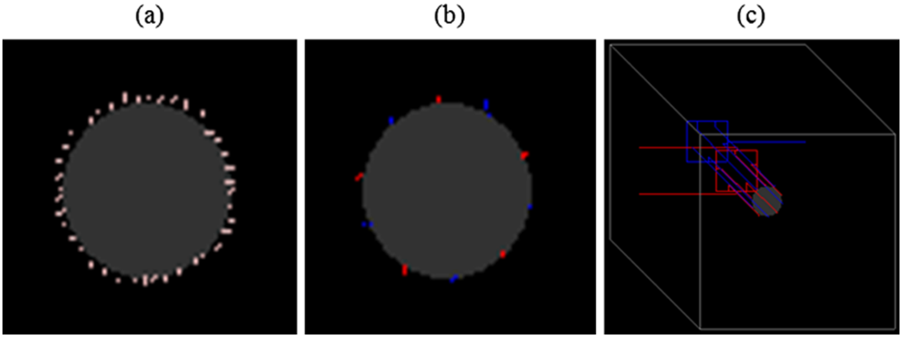

Fig. 4 Initial conditions for all simulations showing (**a**) 40 AC sprouts and (**b**) 10 EC sprouts evenly spaced around the optic nerve, and (**c**) the underlying set-up of parent vessels. In both (**b**) and (**c**), arterial segments are identified in *red*, while venous segments are *blue*

nature and these are distributed evenly around the perimeter of the chiasm in an alternating pattern; the fate of individual endothelial sprouts may already be determined biologically even at this early stage of development (Erber et al. 2006; Davies et al. 2010). All simulations begin at embryonic day E15 (i.e. 6 days before birth), with the initiation of the migratory response of astrocytes—the onset of endothelial cell migration is delayed by 6 days (until birth at E21), in accordance with experimental observations.

PDGF-A, produced by retinal ganglion cells and assumed to have reached a steady-state concentration profile across the RGC plexus prior to astrocyte emergence from the optic nerve, is initialised to zero concentration in the region of the optic nerve head and varies radially according to:

$$p(r,0) = p_{\max} - \beta e^{\frac{-r^2}{\varepsilon}}, \tag{29}$$

elsewhere, where r is the normalised distance from the centre of the optic nerve head ($p_{\max} = 1.0$, $\beta = 0.45$, $\varepsilon = 0.45$). Bound proteins densities (e and f) are initialised to unity and VEGF-A (c) and matrix-degrading enzyme (m_a and m_n) concentrations are all initialised to zero.

The final set of boundary conditions relate to the perfusion model. Prior to endothelial migration, there are no anastomoses on the retinal surface (and consequently no flow), with only disconnected alternating arterial/venous sprout tips present; the former connected to a higher pressure arterial circulation and the latter connected to a lower pressure venous system. In order to keep the two circulations separate until loop formation on the retinal plexus, two additional planes are added below the main simulation domain. The first of these contains only arterial parent vessels that connect each arterial sprout directly to the main *inlet* port of the system (located at the far left of the domain, Fig. 4c). The second additional plane contains only venous parent vessels that connect venous sprouts directly to the main *outlet* of the system (located at the far right of the network). This orderly configuration allows inlet and outlet pressures (P_{in} and P_{out}, respectively) to be controlled independently and guarantees that flow on the retinal surface only begins once endothelial anastomosis has occurred. In addition, the radii of the arterial and venous vessels are assigned a value

(R_{PV}) larger than the maximum possible adapted vessel radii ($R_{\max}$) on the developing plexus, which remains fixed throughout a simulation. This minimises the impact of any heterogeneity in the path lengths travelled and bifurcations negotiated by blood flowing through the parent vessels and ensures a uniform delivery of haematocrit to the capillary plexus, as asymmetric delivery was found to have a highly detrimental effect on the evolution of physiologically realistic capillary structures. On the commencement of flow, blood with a fixed haematocrit (H_D^{in}) and oxygen load (S_V^{in}) is fed into the high pressure arterial inlet. Oxygen concentrations in both the tissue and vessels are initialised to zero and we impose zero-flux tissue oxygen boundary conditions around the domain.

4 Results

A broad spectrum of simulation results is presented in this section, ranging from the relatively straightforward application of the model to astrocyte and endothelial migration, to more involved perfusion-dominated remodelling of the developing vascular plexus. Unless otherwise stated, all of the simulations used the model equations described above, with base-case parameters shown in Table 1 in Appendix A. Note that the base-case simulation utilised a domain size of 4.4 × 4.4 mm (the maximum murine retinal diameter observed up to post-natal day 20), whilst a number of the sensitivities were restricted to a slightly smaller domain size (3 × 3 mm, corresponding to post-natal day 6).

4.1 Astrocyte and Endothelial Migration

As a first benchmarking study, attention is focussed on cellular migration across the RGC plexus, initialised at embryonic day 15 (E15). Note that no flow is included in the model at this stage; the main concern here is the modelling of the cellular fronts observed experimentally. Figure 5 shows the evolution of the astrocyte and endothelial cell networks over the full 4.4 × 4.4 mm domain as they respond to their various guidance cues. The corresponding VEGF-A concentration profiles (produced by astrocytes and degraded by endothelial cells) are shown in Fig. 6. Only astrocyte sprout activity is observed on the RGC plexus prior to birth, producing a dense, highly connected scaffold from the optic nerve chiasm (Fig. 5a) and releasing VEGF-A into the surrounding milieu (Fig. 6a). At day P0, endothelial sprouts begin to migrate chemotactically in response to evolving VEGF-A gradients laid down by the preceding astrocyte tip cells, producing nascent capillary structures that are highly disorganised and excessively branched (Fig. 5b). The astrocyte front reaches the outer periphery of the RGC plexus at approximately post-natal day 5, by which time the capillary plexus has extended approximately halfway across the domain (Fig. 5c). Over this period, the VEGF-A concentration has evolved to produce a radial, wave-like profile travelling outwards into the domain from the optic nerve. Throughout plexus development, the peak of the concentration profile straddles the migrating front of the two cell types—lagging behind the leading edge of astrocytes, but guiding the endothelial cell progression behind (Figs. 6b and 6c). A comparison between experimental

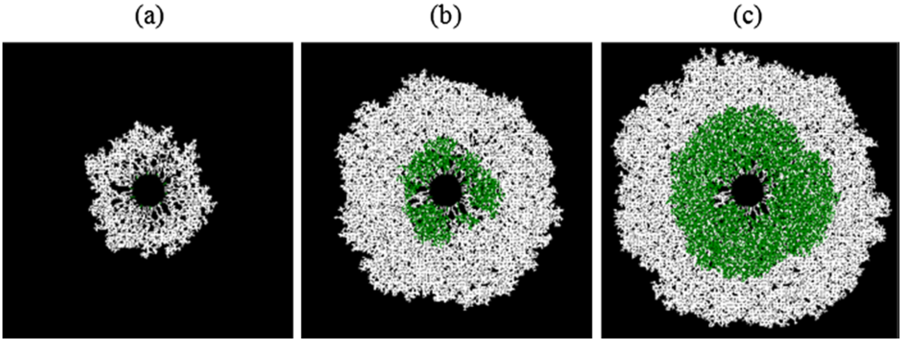

Fig. 5 Growth of the retinal AC network (*white*) and EC plexus (*green*) on a 4.4 × 4.4 mm domain. Migration of ACs begins at E15, while the ECs follow at P0—no flow is considered in this simulation. The snapshots shown here correspond to (**a**) E19.3, (**b**) P2.5 and (**c**) P4.7

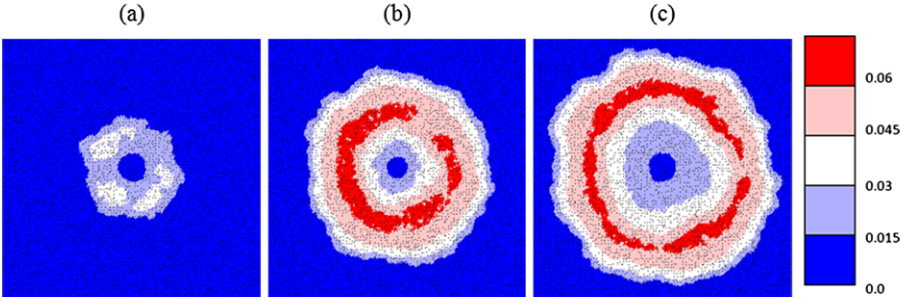

Fig. 6 Evolution of the VEGF concentration profile corresponding to the snapshots of AC and EC migration in Fig. 5

and model data of the temporal development of the two cellular fronts is shown in Fig. 7—the in silico results are found to be in excellent quantitative agreement with the laboratory observations.

4.2 Perfusion and Plexus Remodelling

Whilst the migration results presented in the previous section are useful in establishing a quantitative link between experiment and simulation, they are only concerned with the temporal evolution of astrocyte and endothelial fronts as they migrate across the RGC plexus. The lack of perfusion-related remodelling means that the only heterogeneity in evidence corresponds to the emergence of small acellular islands within the developing plexuses—a manifestation of the stochastic nature of the branching process. However, in vivo retinal vasculatures are highly structured, consisting of alternating vascular trees characterised by a hierarchy of capillary radii (Fig. 2). In order to address this, the introduction of perfusion, oxygen delivery and plexus remodelling is required in the modelling approach as described in Sects. 3.4 and 3.5. The simulation protocol adopted for all subsequent simulations incorporating blood flow is now briefly described.

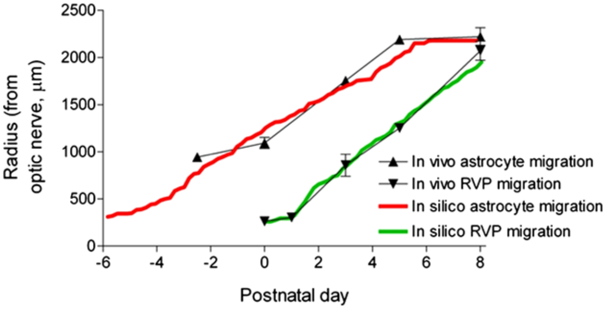

Fig. 7 Plot comparing the rate of frontal advance of ACs and ECs obtained experimentally with those obtained by simulation. AC migration is represented by *triangles with error bars* (in vivo) or a *solid red line* (in silico), while EC migration is represented by *inverted triangles with error bars* (in vivo) or a *solid green line* (in silico)

Each simulation begins at day E15 with the initiation of astrocyte migration from the optic nerve chiasm, followed by the onset of endothelial cell migration at E21/P0. Ideally, capillary beds should be flowed and remodelled whenever a new endothelial anastomosis occurs. However, the computational effort required to undertake this is prohibitive and so some compromise must be reached—a small sensitivity study determined that perfusion of the capillary bed to steady state every 24–30 hours (depending upon domain size) was adequate without compromising the architecture of the final plexus. The first period of flow was chosen to begin around day P2.5, when the EC network is fully connected and of an appreciable size. The volumetric flow rate, blood rheological properties and capillary radius of each individual segment is updated according to the equations described in Sect. 3.4. Once the vascular bed has converged to a steady state, the oxygen delivery equations ((27) and (28)) are solved throughout the domain—these data are then used to remodel (i.e. prune) the capillary network according to the algorithm detailed in Sect. 3.5. This newly pruned network provides the starting point for the next iteration of the angiogenesis model.

4.2.1 Plexus Formation in the Absence of Convected and Conducted Stimuli

As a first attempt towards capturing the flow-induced development of hierarchical vascular structures in the retina, it was decided to incorporate a number of well-documented flow stimuli that have been used previously by the authors (and others) in the contexts of tumour-induced angiogenesis and wound healing. As discussed in Sect. 3.4, this requires the application of (11) rather than (25) for determining vessel dilation or constriction. This simulation was carried out on a reduced domain size of 3 × 3 mm, which naturally restricts the timescale of the simulation as the EC front reaches this domain boundary at around P5 (although this is of no concern to the matter about to be demonstrated). The resulting retinal vasculature is shown in Fig. 8—a self-reinforcing capillary shunt develops (Fig. 8a), regardless of the extent of the outwardly growing plexus. Consequently, a non-zero haematocrit is restricted to a region proximal to the optic nerve (Fig. 8b), and oxygen delivery to the retinal plexus is greatly restricted (Fig. 8c). Such a dramatic dilation of peripheral vessels is

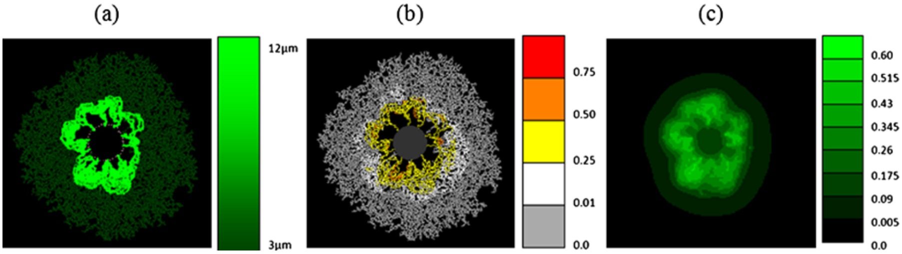

Fig. 8 Snapshots at P4.7 from a vasculature which has undergone three cycles of growth, flow, oxygen delivery and pruning on a 3 × 3 mm domain. The angio-adaptation algorithm applied here is described by (11)—the particular parameters used can be found in Table 2 of Appendix A. Specifically, the images show (**a**) vessel radii, (**b**) haematocrit and (**c**) tissue oxygen concentration

not characteristic of wild-type retinae—the wild-type mathematical model is clearly lacking some important shunt-prevention mechanisms at this stage. A detailed discussion of shunt prevention was presented earlier in Sect. 3.4 and so the final phase of development involves the inclusion of the latest flow-based stimuli as reported by Pries and co-workers (Pries et al. 2001, equations (18)–(22)) into the perfusion model.

4.2.2 Plexus Formation Incorporating Convected and Conducted Stimuli

The base-case simulation using the complete model is presented in Fig. 9 (employing the full 4.4 × 4.4 mm domain). Each figure highlights the behaviour of a particular model component throughout the development of the retinal capillary plexus: from the commencement of flow at approximately day P2.5 until the network approaches the boundaries of the domain at day P8. Specifically, figures show the post-flow, steady-state distribution of capillary architecture, haematocrit distribution, vessel oxygen concentration, tissue oxygen concentration, and areas of capillary remodelling (i.e. pruning—an additional graphic highlighting the specific position of each pruned vessel segment, and the specific time point at which it was removed).

The progression of the underlying astrocyte network—and the associated VEGF-A gradients left in their wake (shown earlier in Figs. 5 and 6)—provides a crucial mechanistic link between the initial stages of retinal development (viz. the formation of the RGC plexus) and the later sequestration and development of a capillary vessel network. It is apparent that the astrocyte front moves rapidly away from the optic nerve chiasm and simultaneous VEGF-A production creates a travelling wavefront, with the peak concentration lying behind the migrating tip cells. EC migration commences at P0, with subsequent growth largely driven by the chemotactic response to the VEGF-A gradients trailing an outward-moving maximum. During the first period of flow at day P2.7, angio-adaptation, oxygen delivery and vessel remodelling are already taking place throughout the nascent capillary network (Figs. 9a, 9j, 9m). A striking feature of the haematocrit distribution at this early stage of development is its large degree of spatial heterogeneity within the network (Fig. 9d), largely determined by the process of phase separation at bifurcations. Almost every capillary element carries some level of haematocrit, suggesting that the extreme phenomenon

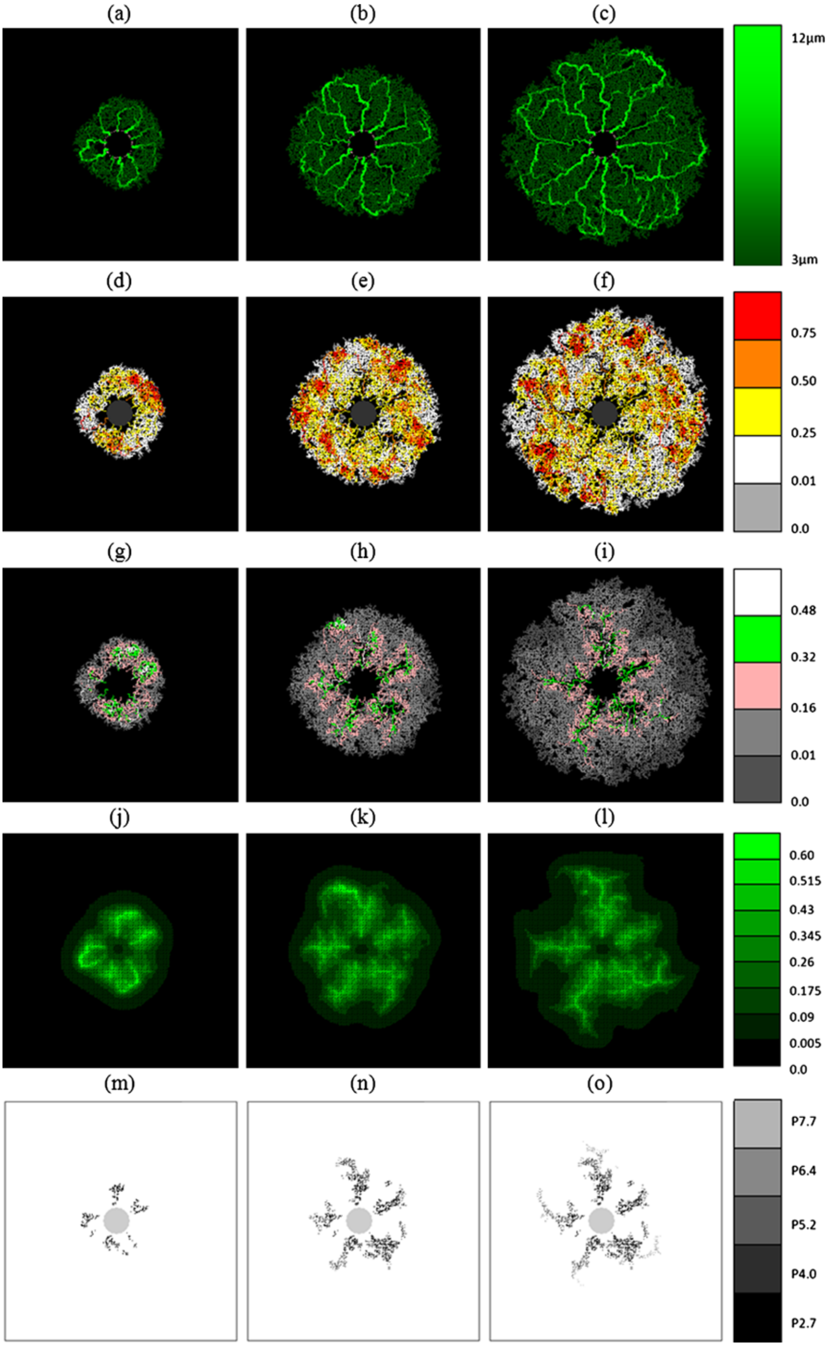

Fig. 9 Snapshots of a developing retinal vascular plexus on a 4.4 × 4.4 mm domain showing (**a**–**c**) vessel radii, (**d**–**f**) haematocrit, (**g**–**i**) vessel oxygen concentration, (**j**–**l**) tissue oxygen concentration and (**m**–**o**) pruned capillary segments. Each column corresponds to a particular time point, namely (from *left* to *right*) P2.7, P5.2 and P7.7. Images from intermediate days have been omitted

of total plasma skimming is largely absent within the dense mesh of vessels. We also note the presence of a number of vessel segments characterised by haematocrits exceeding 0.75, occurring mainly in two small pockets near the leading edge of the plexus (remember that the input haematocrit was 0.45, indicating a concentrating effect in RBCs as blood flows to more distal areas of the retina). This result correlates well with the work of Ganesan et al. (2010), who observed simulated haematocrit values approaching 0.8 in equatorial vessel segments using an image-based network model of the fully developed murine retinal vasculature. In Figs. 9g and 9j we show the vessel oxygen and the tissue oxygen distributions, respectively. The vessel oxygen distribution closely follows that of the haematocrit, as does the distribution of oxygen tension within the tissue. As a consequence of blood flow and local oxygen tensions, a structured vasculature begins to emerge from the originally homogeneous capillary bed (Fig. 9a), with a number of the arteries tentatively forming dilated anastomoses with each of their neighbouring veins. Even at such an early stage of development, this realistic looking network clearly constitutes a significant improvement on that presented in Fig. 8, emphasising the requirement for the introduction of shunt-preventing stimuli into the angio-adaptation algorithm. It is also possible to observe the onset of oxygen-induced vascular pruning at this stage, particularly around the uppermost artery, where a small capillary-free zone develops. For clarity, each pruned capillary segment is shown in Fig. 9m. At this early time, only a small amount of pruning is seen, accentuating the presence of the small dilated arterio-venous loops.

After each 30 hours of growth, the simulated vasculature undergoes a cycle of flow, oxygen transport and remodelling. For brevity, we exclude simulation images from intermediate days and proceed immediately to consider the retinal plexus at P5.2 (after the third cycle of perfusion). The dynamic nature of capillary plexus development can be inferred from a comparison between Figs. 9a and 9b. The small dilated loops prevalent near the optic nerve chiasm at earlier times are remodelled as the vascular bed grows: the sensitivity of the shunt-preventing stimuli to changes in the network architecture is emphasised by the emergence of larger arterio-venous loops that serve to transport blood efficiently towards peripheral regions of the domain. An interesting natural consequence of the angio-adaptation model is that the radii of arterial inlet segments evolve to be consistently smaller than their venous outlet counterparts (Fig. 9b). This corresponds to the results obtained by Ganesan et al. (2010) who used a combination of measurements from confocal scanning microscopic images and the optimisation principle of Murray's law to quantify the diameter of each vessel segment of the murine superficial RVP. The haematocrit distribution throughout the plexus is again seen to be highly heterogeneous at day P5.2 (Fig. 9e). Although a large percentage of capillaries carry a level of red blood cells below the input haematocrit value, localised regions towards the retinal equator (i.e. away from the optic nerve) once again exceed 0.75. However, in contrast to day P2.7, haematocrit is no longer highly correlated with the vessel oxygen profile (Fig. 9h) and many of the high haematocrit regions of the capillary bed display low vessel oxygen concentrations—remember that haematocrit refers to RBC concentration and does not necessarily imply that these RBCs are highly oxygenated. Due to the increased plexus size, and the limited capacity of narrow capillaries to supply oxygen to equatorial regions, much of the oxygen transported transmurally from vessel to tissue occurs proximal to the arterial sources. Furthermore, it is clear from the tissue oxygen profile (Fig. 9k) that the majority of oxygen is supplied by the dilated anastomoses, with oxygen tensions dipping significantly as the venous sinks are approached. Vascular remodelling up to day P5.2 is presented in Fig. 9n—capillary pruning is prominent around each of the five inlet arteries and is particularly noticeable around the uppermost artery (extending along the length of the arterial section and decreasing as the more hypoxic venous section is traversed).

The final time period covered by the base-case simulation ends at post-natal day 7.7 (P7.7) and corresponding results demonstrate the significant role played by flow and vascular remodelling in determining the final form of the retinal vasculature (Fig. 9c). The removal of many of the smaller capillaries on either side of the main arterial vessels increases their prominence as major flow pathways, ensuring that they are retained as the network continues to expand towards the edge of the RGC plexus. The emergence of a highly structured network architecture has a large impact on the distribution of retinal haematocrit (Fig. 9f). The regions of greatest haematocrit are situated in the vicinity of the dilated arterio-venous loops, whilst lower haematocrit values characterise regions lying between the main vessels (a manifestation of the phase separation effect). The haematocrit increases downstream of each bifurcation on the arterial side, peaking at the retinal equator before gradually decreasing towards the outlet veins. Again we see a similarity to the work of Ganesan et al. (2010) who observed the same behaviour, albeit in a sparser, three-layer fully developed retinal vascular network. Under the assumption that red blood cells are the primary source of oxygen in the system, this phenomenon also has interesting implications for the delivery of oxygen from the vasculature to the tissue. Since the oxygen is fed into the network at a constant concentration and leaves the vessels transmurally as it flows downstream, the absence of phase separation would cause a decreasing gradient of vessel oxygen concentration as we move downstream through bifurcating arterial trees—starving the outer regions of the retina of oxygen. However, phase separation actually leads to an *increasing* gradient of haematocrit away from the optic nerve, with the result that peak tissue and vessel oxygen tensions can occur far away from the network inlets. Such a result was not observed in the work of Liu et al. (2009) who examined the distribution of oxygen partial pressure in a human arterial retinal network. This is due to the absence of phase separation in their model, which they attribute to the lack of research in this field for human vasculatures. It is likely, due to the larger diameter of the vessels involved, that the effects of phase separation would be less prominent than found here in the murine case.

One of the most involved aspects of the modelling process is the calculation of the pressure field for such a complex (and evolving) network topology. Two additional planes were added below the main simulation domain: the first of these contains only arterial parent vessels and a looped manifold that connects each arterial sprout directly to the main inlet ports of the system (Fig. 4c). The second additional plane contains only venous parent vessels and a looped venous manifold that connects venous sprouts directly to the main outlet of the system. This methodical arrangement allows inlet and outlet pressures to be controlled independently. The pressure field corresponding to the superficial retinal vasculature at post-natal day 7.7 is shown in Fig. 10a—high pressure arterial regions are seen to fan out from the optic nerve

Fig. 10 Quantification of the pressure distribution underlying the vasculature of Figs. 9c, 9f, 9i. Specifically, the images show (**a**) contour plot of the nodal pressures on the superficial retinal vascular plexus, and (**b**) azimuthal pressure variations at the distances 0.5 mm (*blue*), 1.0 mm (*red*) and 1.5 mm (*green*) from the optic nerve centre

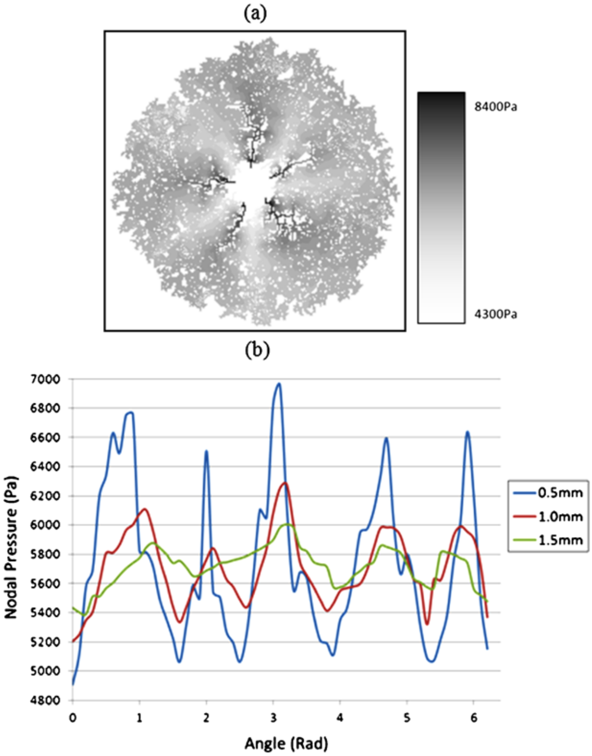

chiasm towards the retinal equator, interspersed with radiating low-pressure areas. The figure gives a useful insight into the global dispersal of perfusing nutrients during retinal development and could also inform the application of future therapeutic interventions. A more quantitative analysis of the pressure distribution is shown in Fig. 10b. The periodic nature of the arterio-venous pressures measured azimuthally at distances of 0.5 mm, 1.0 mm, and 1.5 mm from the centre of the domain is self-evident, with the amplitude of the pressure variations highest close to the optic nerve and progressively damped towards the edge of the domain.

Having successfully anchored the mathematical model to the available experimental data, a number of sensitivity analyses were next carried out to investigate the impact of a number of potential pathological or transgenic cases which may impede normal development. Of course there are many parameters in the model that could be varied, leading to a wide variety of outcomes, but here attention is focussed on those parameters that can be directly correlated with murine retinal pathologies. In the interests of computational efficiency we reduce the domain size to 3×3 mm, and simulate a new base case with which to make relevant comparisons. As mentioned earlier, this restricts the timescale of the simulation to a maximum of around 5 days post-birth. For the sensitivities shown, however, this is sufficient time to appreciate the impact of the various parameter perturbations. The vasculature presented in each case is the end point of 3 cycles of growth, flow, angio-adaptation, oxygen delivery and remodelling.

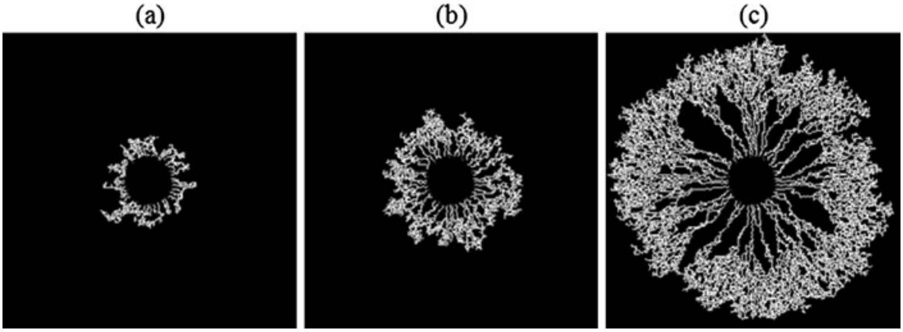

Fig. 11 Snapshots at E17.7 displaying the AC network on a 3 × 3 mm domain for a range of AC chemotaxis coefficient (χ_p) values. The particular values considered were (**a**) 0.018, (**b**) 0.18 (base-case parameter) and (**c**) 1.8

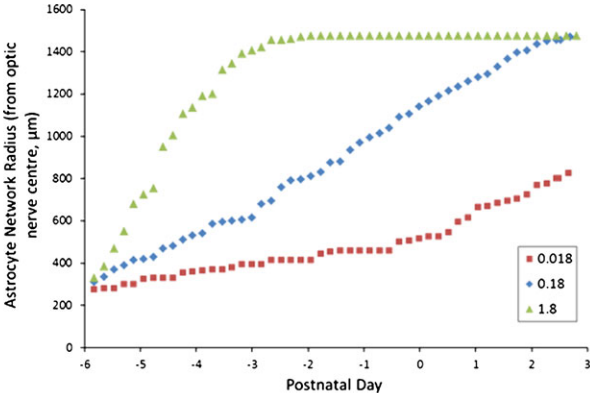

Fig. 12 Plot comparing the rate of AC frontal advance for each simulation in Fig. 11. The series correspond to the AC chemotaxis coefficient (χ_p) values 0.018 (*blue diamonds*), 0.18 (*red squares*) and 1.8 (*green triangles*). The plot terminates around P3, when the base-case AC network ($\chi_p = 0.18$) reaches the domain boundary

4.2.3 Aberrant Plexus Formation I—Astrocyte Chemotaxis

The first sensitivity carried out using the model examined the impact of the underlying astrocyte plexus upon the subsequent migration of endothelial cells during angiogenesis. The chemotactic response of astrocytes to PDGF (secreted by the retinal ganglion cells at an earlier stage of development) was varied through the parameter χ_p in (1). A tenfold decrease and increase in the chemotactic parameter was investigated and the resulting astrocyte networks at embryonic day E19.3 (i.e. prior to the onset of angiogenesis) are shown in Fig. 11. As the chemotactic response of the astrocytes is varied, the plexus architecture changes markedly. Suppressed chemotaxis produces a slow-growing, dense astrocyte scaffold, whilst enhanced chemotaxis results in a rapidly growing network that is a good deal sparser across half of the domain. The evolution of the astrocyte fronts from day E15 through to day P3 are shown graphically in Fig. 12. Perhaps the most interesting aspect of the sensitivity, however, is the effect that astrocyte chemotaxis has on retinal VEGF-A concentrations and angiogenesis. Figure 13 shows VEGF-A concentration contours and capillary networks at post-natal day P4.7. VEGF-A is produced by hypoxic astrocytes, and so the onset of angiogenesis begins to switch off its production in areas of the domain

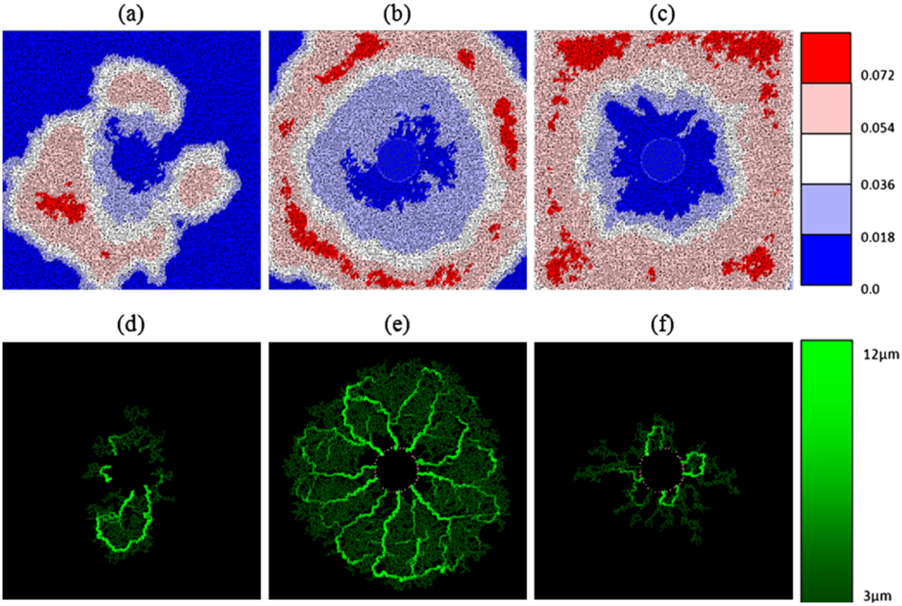

Fig. 13 Snapshots at P4.7 displaying the VEGF concentration profiles (**a**–**c**) and vessel radii distributions (**d**–**f**) corresponding to the AC scaffolds previewed in Fig. 11. As above these were generated on a 3 × 3 mm domain using the AC chemotaxis coefficient (χ_p) values 0.018 (**a**, **d**), 0.18 (**b**, **e**) and 1.8 (**c**, **f**)

that are perfused with oxygen-rich blood. The results predict that retinal development would be most damaged if the underlying astrocyte scaffold was produced too rapidly (i.e. under conditions of increased chemotactic sensitivity to PDGF). In this case, VEGF-A is only produced in reasonable quantities close to the retinal periphery (where the density of hypoxic astrocytes is substantial, Fig. 13c). The paucity of astrocytes proximal to the optic nerve means that VEGF-A gradients there are woefully inadequate in providing chemotactic support for the emerging endothelial cells—the resulting vascular plexus is substantially compromised (Fig. 13f).

Although no direct in vivo studies of astrocyte *chemotaxis* appear to have been reported to date, pathologically the sensitivity can be related to observations in transgenic mouse models where PDGF-A is over-expressed by RGC or astrocytes (Fruttiger et al. 1996; West et al. 2005). In these experimental systems, astrocyte numbers are found to increase with increased concentration of PDGF-A, yet migration is suppressed. This suggests that a domain rich in PDGF-A could act as a promoter of astrocyte mitosis, whilst simultaneously saturating any chemotactic response.

4.2.4 Aberrant Plexus Formation II—VEGF-A Isoform

The second sensitivity considered is the impact of varying the specific VEGF-A isoform produced by the astrocytes. Variations in the diffusive properties of different VEGF-A isoforms are well documented and a number of murine transgenic mouse models specifically expressing a single isoform have been reported in the literature (Mitchell et al. 2006; Rutland et al. 2007). It has been shown that higher molecular

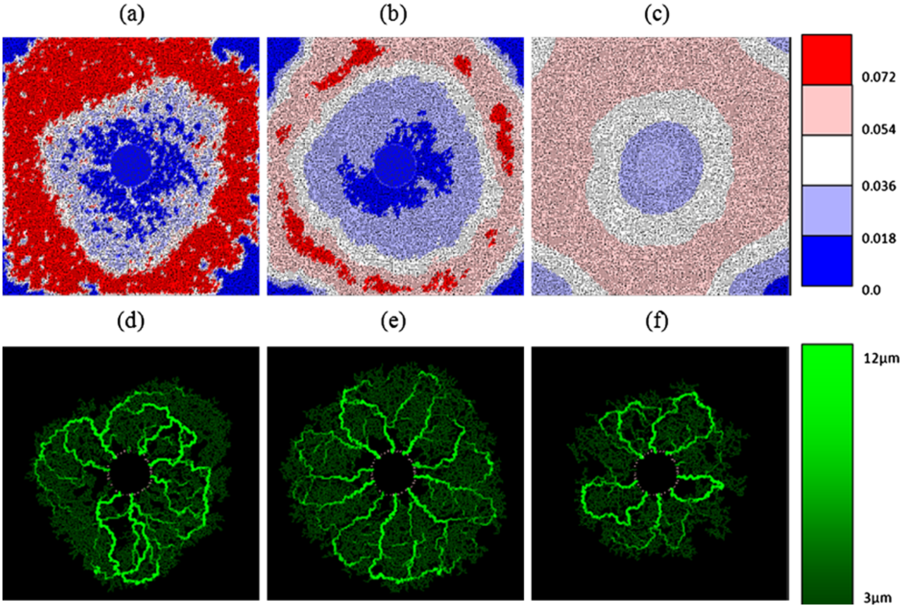

Fig. 14 Snapshots at P4.7 displaying the VEGF concentration profiles (**a**–**c**) and vessel radii distributions (**d**–**f**) on a 3 × 3 mm domain for a range of VEGF diffusion coefficient (D_c) values. The particular values considered were (**a**, **d**) 0.0005, (**b**, **e**) 0.005 (base-case parameter) and (**c**, **f**) 0.05

weight compounds are closely correlated with reduced diffusion within the matrix and increased binding tendency. In order to investigate the implications of this aspect of isoform behaviour on capillary migration, the in silico model was run for different values of VEGF-A diffusion coefficient (D_c). The resulting networks at day P4.7 are shown in Fig. 14, where reduced VEGF-A diffusion results in more localised pooling of VEGF-A and shallower concentration gradients (compare Figs. 14a and 14b). The reduction in VEGF-A diffusion consequently leads to a weaker angiogenic response (Fig. 14d, which is also partly attributable to the reduced chemotactic sensitivity at high VEGF-A concentrations through (4)). Interestingly, an increase in VEGF-A diffusion also results in a slower rate of capillary growth. Although the initial rate of expansion parallels that seen in the base-case simulation, increased diffusion results in a shallower overall VEGF-A profile and lower concentrations at the leading edge (Fig. 14c). Consequently, both chemotaxis and capillary branching are impaired, resulting in a highly irregular vascular network and numerous unperfused islands of retinal tissue (Fig. 14f). The sensitivity results support the notion that the base-case VEGF-A diffusion coefficient is optimum in producing a rate of capillary plexus expansion that is perfectly consistent with wild-type angiogenesis in the retina. The results clearly show that the dominant VEGF-A isoform (VEGF-A_{164} in the mouse, Mitchell et al. 2006) has a profound effect upon retinal development through its interaction with migrating endothelial cells during angiogenesis. The model predicts that isoforms such as VEGF-A_{120} could be expected to result in the formation of numerous poorly branched large diameter vessels, similar to the in vivo observations of Mitchell et al. (2006), whilst higher molecular weight isoforms such as VEGF-A_{188}

would lead to the formation of large dilated vascular sacs, which have previously been reported in VEGF$_{188}$ mice by Rutland et al. (2007).

4.2.5 Aberrant Plexus Formation III—Haematocrit and Oxygen Consumption

The final series of simulations examines the importance of oxygen supply to the retina during angiogenesis. Two parameters have been varied in the model: input arterial haematocrit (with the corresponding variation in input arterial vessel oxygen concentration) and tissue oxygen consumption rate. An increased haematocrit is often symptomatic of hyperoxic conditions, whilst a reduced rate of oxygen consumption is symptomatic of reduced metabolism. Simulation results at day P4.7 for increased input haematocrit ($H_D^{\mathrm{in}} = 0.6$) and decreased oxygen uptake ($\sigma_{ST} = 0.002\ \mathrm{s}^{-1}$) are shown in Fig. 15—base-case results are also presented for visual comparison. An increased haematocrit leads to the persistence of high RBC concentrations throughout dilated arterio-venous loops; the impact of phase separation at capillary junctions is less pronounced (Fig. 15e). Consequently, the main arterio-venous loops maintain higher local oxygen concentrations, resulting in higher tissue oxygen tensions in the vicinity of all major vessels and extensive capillary remodelling (Figs. 15f and 15g). This ultimately causes substantial capillary-free zones to appear within the plexus and a state of hyperoxia is found to persist throughout retinal development; a situation that is replicated in the clinically significant condition of retinopathy of prematurity (Stout and Stout 2003). This phenomenon is further amplified under conditions of reduced oxygen consumption (Figs. 15i–15l). Here, the entire retinal domain becomes flooded with oxygen and capillary-free zones are pervasive. These observations are similar to mouse models of oxygen-induced retinopathy. In this experimental model, neonatal mice are placed in a high oxygen environment, which leads to an increased arteriolar oxygen concentration. Conversely, the region of the retina within the oxygen diffusion limit of larger arterioles in the optic nerve becomes hyperoxic, VEGF-A is downregulated, endothelial plexus formation is inhibited and retinal vessel segments are obliterated (West et al. 2005; Weidemann et al. 2010).

5 Discussion and Conclusions

The spatio-temporal evolution of nascent capillary networks during development is a key regulator of tissue patterning and function and it is important to understand the important roles played by cellular and molecular cues throughout the angiogenic process. The growth and differentiation of the mammalian neural retina is dependent upon the formation of a multi-layered, interlinked vascular supply, and provides an excellent in vivo system for investigating angiogenesis. It represents an exquisitely balanced dynamic process from the field of developmental biology that is an excellent target for mathematical modelling. The in silico RVP structures resulting from this study have been compared with corresponding experimental data at various stages of development and excellent agreement has been demonstrated.

Fig. 15 Snapshots at P4.7 of three different scenarios simulated on a 3 × 3 mm domain. Images (**a**–**d**) show the base-case (parameter values $H_D^{\mathrm{in}} = 0.45$ and $\sigma_{ST} = 0.02$), while (**e**–**h**) demonstrate the outcome of increasing inlet haematocrit ($H_D^{\mathrm{in}} = 0.6$) and (**i**–**l**) display the result of reducing oxygen consumption ($\sigma_{ST} = 0.002$). In each case the images display (**a**, **e**, **i**) haematocrit, (**b**, **f**, **j**) tissue oxygen concentration, (**c**, **g**, **k**) pruned capillary segments and (**d**, **h**, **l**) vessel radii

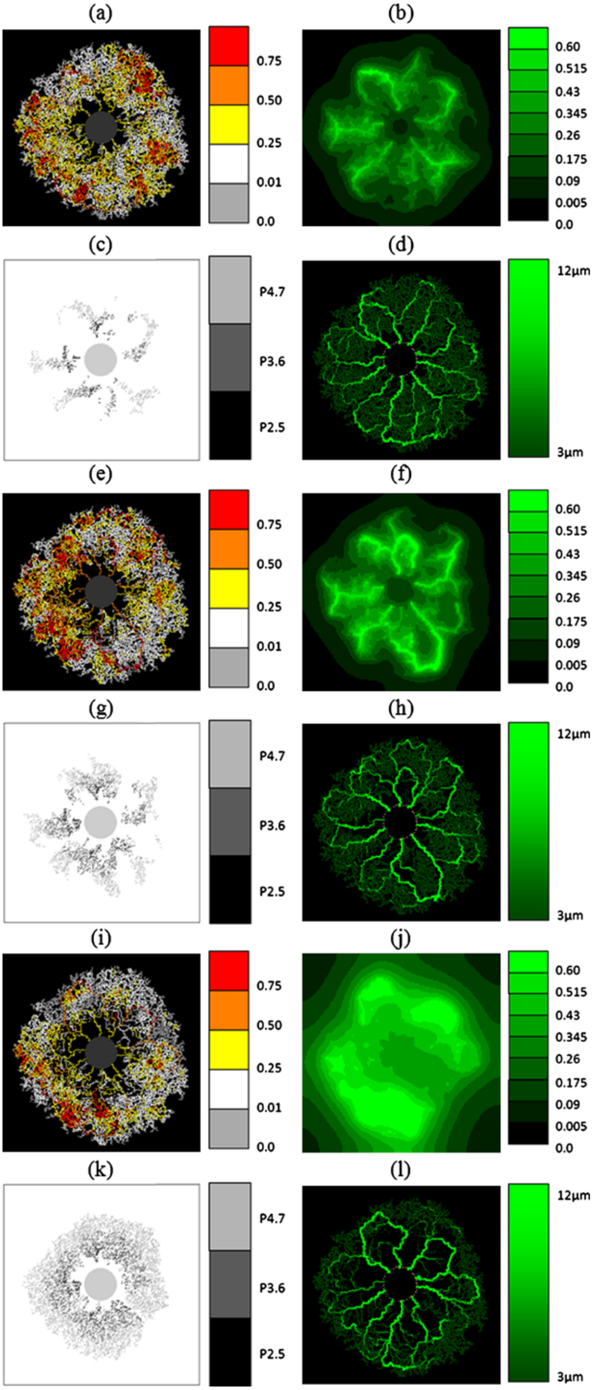

Retinal vascular plexus development begins with the emergence of astrocytes from the optic nerve region at embryonic day 15.5, which migrate in response to a chemotactic gradient of PDGF-A produced by a pre-existing underlying layer of retinal ganglion cells (RGCs). Migrating astrocytes branch in response to PDGF-A, assume a stellate phenotype, and form a dense astrocyte mesh that forms the foundation for the subsequent expansion of the capillary network. During the formation of the astrocyte scaffold, hypoxic astrocytes secrete the growth factor VEGF-A, which acts as the primary chemoattractant for endothelial cells, facilitating their migration across the plexus and leading to the growth of a retinal vasculature. These migratory mechanisms had been considered in a previously reported one-dimensional study of retinal angiogenesis by Aubert et al. (2011), which successfully reproduced the frontal velocities of astrocytes and endothelial cells as they migrated across the superficial retinal plane. However, this approach was, by definition, unable to generate spatial information for the entire retinal surface and a more realistic two-dimensional hybrid PDE-discrete model has been derived here, in order to track the migration of individual astrocyte and endothelial tip cells towards the outer retinal boundary.

It is important to recognise that the developing RVP is not an inert structure; the vascular bed adapts and remodels in response to a wide variety of metabolic and chemical stimuli. Hence, the complex hierarchical arrangements observed in vivo in the retina can never be reproduced using simple migration equations alone: perfusion-modified vessel adaptation and remodelling mechanisms must be included. Earlier approaches to vascular adaptation have proved successful in qualitatively reproducing vasculatures in the contexts of tumour-induced angiogenesis and wound healing (McDougall et al. 2002, 2006; Stephanou et al. 2005, 2006; Macklin et al. 2009; Owen et al. 2009b; Welter et al. 2008, 2009; Machado et al. 2010). However, it has been demonstrated here that the retina poses a more rigorous test of any angiogenesis model, and more refined perfusion-related stimuli based upon the latest developments in vascular research must be included to fully capture the intricacies of the in vivo observations. These include phase separation of plasma and red blood cells at capillary junctions in the microvasculature, and oxygen-dependent "conducted" and "convected" stimuli (as reported by Pries et al. 1989, 2001, respectively; see also Pries et al. 2010 for a review). Whilst such phenomena are relatively straightforward to incorporate into simple bifurcating networks (see, for example, Secomb et al. 2007 for details of a similar approach dealing with the interaction between angiogenesis, remodelling and capillary pruning, although not in the specific context of the murine retinal vasculature), *pre-pruned* vascular plexuses associated with the developing retina are not so hierarchical. Consequently, here the formulations have been extended to include non-uniform combinations of vessel connectivity, flow direction, parent and daughter vessel diameter, and parent vessel discharge haematocrit. This new generalisation is more widely applicable to heterogeneous vascular architectures, whilst maintaining the key features of the hierarchical model. To reiterate, the inclusion of these refined mechanisms in earlier treatments of angiogenesis modelling has been somewhat lacking for understandable reasons; their addition has been computationally prohibitive in large networks and the concentration tracking algorithms required in topologically complex situations become rather involved; however, it has been shown here that the impact of these two new stimuli can be substantial.

Throughout the modelling work, it has been imperative that the approach should be firmly coupled to the experimental biology and to this end, we have attempted to honour the underlying cellular and vascular processes as closely as possible. The main focus of the investigation has been to understand how the various cellular, molecular, and metabolic cues regulate RVP growth and form in both wild-type and transgenic situations. A broad spectrum of simulation results has been presented, ranging from the relatively straightforward application of the model to astrocyte and endothelial migration, to more involved perfusion-dominated remodelling of the developing vascular plexus. The main outcomes of the study have been the following:

- Model data concerning the temporal development of the astrocyte and endothelial cellular fronts were found to be in excellent quantitative agreement with the laboratory observations.
- A large degree of spatial heterogeneity in haematocrit within the capillary plexus was noted, with some distal areas of the retina containing haematocrit values exceeding 0.75—a considerable increase on the input value of 0.45 and caused predominantly by the process of phase separation (and concomitant concentration of downstream RBCs) at capillary junctions.
- Phase separation leads to an *increasing* gradient of haematocrit away from the optic nerve, with the beneficial result that peak tissue and vessel oxygen tensions can occur far away from the network inlets.
- Suppressed astrocyte chemotaxis was found to produce a slow-growing, dense astrocyte scaffold, whilst enhanced astrocyte chemotaxis resulted in a rapidly growing, sparse network. The model predicted that retinal vascular development would be most damaged if the underlying astrocyte scaffold was produced too rapidly (i.e. under conditions of increased chemotactic sensitivity to PDGF-A). Experimentally, over-expression of PDGF-A in transgenic mice has been shown to reduce the extent of astrocyte migration in neonatal mice (Fruttiger et al. 1996; West et al. 2005), suggesting astrocyte migration is dependent on a gradient of PDGF-A, and the modelling results presented here are highly consistent with this observation.
- Different isoforms of VEGF-A have different molecular weights and a varying ability to bind heparin residues in the extracellular matrix or diffuse freely (Ferrara et al. 1992; Keyt et al. 1996; Park et al. 1993; Shima et al. 1996). Reduced VEGF-A diffusion resulted in extensive localised pooling of VEGF-A close to the optic nerve, mitigating the formation of extensive concentration gradients, and leading to a weaker global angiogenic response (also partly attributable to the reduced chemotactic sensitivity at high VEGF-A concentrations). Interestingly, an *increase* in VEGF-A diffusion also led to a lower rate of capillary growth. These results clearly demonstrate that the dominant VEGF-A isoform has a profound effect upon retinal development through its interaction with migrating endothelial cells during angiogenesis (Gerhardt et al. 2003; Mitchell et al. 2006; Rutland et al. 2007).
- An increased input haematocrit was found to cause persistence of high RBC concentrations throughout dilated arterio-venous loops (phase separation at capillary junctions being less effective in this case). The main arterio-venous loops consequently maintained high local oxygen concentrations, causing the elimination of VEGF-A production by the underlying astrocytes, and extensive cap-

illary remodelling. This condition is further amplified under conditions of reduced oxygen consumption, parallelling the vascular pathology observed in human retinopathy of prematurity (Stout and Stout 2003) and murine models of this disease (Scott et al. 2010; Claxton and Fruttiger 2003; Dorrell et al. 2010; Stone et al. 1996).

A major advantage in studying the retinal vasculature is that it provides a capillary system that can be observed with relative clarity both in vivo and post mortem and, although a complete understanding of the *developing* retinal circulation is still lacking, it provides an excellent target for both theoretical and in silico studies. It also poses a more rigorous test of angiogenesis modelling than, say, tumour-induced angiogenesis, in that the retinal structures exhibit a level of hierarchical patterning that is generally absent from tumour-induced vasculatures. Of course, it should be acknowledged that the retina is not strictly a simple two-dimensional structure and that, in addition to the superficial RVP considered here, two deeper RVP layers form through vertical sprouting from the superficial plexus as the retina expands. The application of the model to investigate the development of these additional layers has not been explicitly considered here but will be the focus of a future study.

Acknowledgements The authors gratefully acknowledge financial support from the BBSRC: Grant # BB/F002254/1 and BB/F002807/1.

Appendix A

Table 1 Parameter values used in all base-case simulations

Parameter	Definition	Value
D_n	EC random motility coefficient	0.00018
χ_c	EC chemotaxis coefficient	0.4
ξ_c	EC chemotactic receptor saturation factor	0.6
ρ_f	EC haptotaxis coefficient	0.0125
D_a	AC random motility coefficient	0.00018
χ_p	AC chemotaxis coefficient	0.18
ξ_p	AC chemotactic receptor saturation factor	0.6
ρ_e	AC haptotaxis coefficient	0.0125
D_c	VEGF diffusion coefficient	0.005
η_c	VEGF uptake rate by EC tips	0.1
σ_c	VEGF decay rate	5.0
α_c	VEGF production rate by hypoxic ACs	3.5
D_p	PDGF diffusion coefficient	0.0025
η_p	PDGF uptake rate by ACs	0.1
σ_p	PDGF decay rate	3.0
D_{m_a}	MDE diffusion coefficient	0.001

Table 1 (*Continued*)

Parameter	Definition	Value
α_{m_a}	MDE production rate by AC tips	0.00001
σ_{m_a}	MDE decay rate	3.0
D_{m_n}	MDE diffusion coefficient	0.001
α_{m_n}	MDE production rate by AC tips	0.00001
σ_{m_n}	MDE decay rate	3.0
β_f	ECM production rate by AC tips	1.5
γ_f	ECM degradation rate	0.1
β_e	ECM production rate by AC tips	1.5
γ_e	ECM degradation rate	0.1
μ_{plasma}	Bulk plasma viscosity	1.2×10^{-3} Pa s
H_D^{in}	Inlet haematocrit value	0.45
S_V^{in}	Inlet vessel oxygen concentration	0.45
D_{ST}	Oxygen diffusion coefficient	2.5×10^{-10} m^2/s
σ_{ST}	Oxygen consumption rate	0.02 s^{-1}
K	Vessel permeability to oxygen	2.5×10^{-4} m/s
$S_{T\text{crit}}$	Critical tissue oxygen concentration for pruning	0.38
A_{crit}	Critical vessel age for pruning	1 day
P_{in}	Inlet arterial blood pressure	10660 Pa (4.4 mm domain) 9860 Pa (3 mm domain)
P_{out}	Outlet venous blood pressure	2060 Pa
$R_{\min}$	Minimum permissible vessel radius	3.0×10^{-6} m
$R_{\max}$	Maximum permissible vessel radius	1.2×10^{-5} m
R_{PV}	Radius of all arterial and venous parent vessels	1.4×10^{-6} m
k_s	Natural shrinking rate of vessels	1.7
k_p	Relative intensity rate of the pressure stimulus	0.8
k_m	Relative intensity rate of the convected stimulus	0.5
k_c	Relative intensity rate of the conducted stimulus	2.6
J_0	Saturation constant for the conducted stimulus	250
τ_{ref}	Reference wall shear stress	0.5 dyn/cm^2
Q_{ref}	Reference flow rate	1.0×10^{-18} m^3/s
$(QH_D)_{\text{ref}}$	Reference RBC flow rate	6.75×10^{-14} m^3/s
L_c	Length constant for conducted stimulus decay	0.01 m

Table 2 Parameter values used in Fig. 9 (all other relevant values unchanged)

Parameter	Value
k_s	0.35
k_p	0.1
k_{metab}	0.07
τ_{ref}	0.103 dyn/cm^2
Q_{metab}	1.9096×10^{-11} m^3/s

We require some further details to explain the process of EC and AC sprout branching. At the beginning of the simulation each initial sprout is set to have an age of zero, but this is supplemented by also assigning each sprout a random time point in its cell cycle. Upon each subsequent occurrence of branching, we assume that one new sprout maintains the direction of its parent sprout while the other sprout direction is chosen randomly. In the former, we set the age of the sprout, and its cell cycle position, to be zero. In the latter, we again set the sprout age to zero, but here we assign a random cell cycle position. We define an additional two parameters, namely a threshold age for branching ($t_{\mathrm{branch}} = 0.076$ days) and a mitosis time describing the length of the cell cycle ($t_{\mathrm{mitosis}} = 0.709$ days). In order for branching to occur, both the age of the parent sprout and its individual cell cycle time must exceed these critical values. In addition to this, the probabilities of AC and EC branching are related to the concentrations of PDGF and VEGF, respectively.

References

Alarcon, T., Byrne, H., & Maini, P. K. (2003). A cellular automaton model for tumour growth in inhomogeneous environment. *J. Theor. Biol.*, *225*(2), 257–274.

Alarcon, T., Owen, M. R., Byrne, H. M., & Maini, P. K. (2006). Multiscale modelling of tumour growth and therapy: the influence of vessel normalisation on chemotherapy. *Comput. Math. Methods Med.*, *7*(2–3), 85–119.

Anderson, A. R. A. (2005). A hybrid mathematical model of solid tumour invasion: the importance of cell adhesion. *IMA J. Math. Med. Biol.*, *22*, 163–186.

Anderson, A. R. A., & Chaplain, M. A. J. (1998). Continuous and discrete mathematical models of tumour-induced angiogenesis. *Bull. Math. Biol.*, *60*, 857–899.

Anderson, A. R. A., Chaplain, M. A. J., Newman, E. L., Steele, R. J. C., & Thompson, A. M. (2000). Mathematical modelling of tumour invasion and metastasis. *J. Theor. Med.*, *2*, 129–154.

Aubert, M., Chaplain, M. A. J., McDougall, S. R., Devlin, A., & Mitchell, C. A. (2011). A continuous mathematical model of the developing murine retinal vasculature. *Bull. Math. Biol.*, *73*, 2430–2451.

Baron, M. (2003). An overview of the notch signalling pathway. *Semin. Cell Dev. Biol.*, *14*, 113–119.

Bauer, A. L., Jackson, T. L., & Jiang, Y. (2007). A cell-based model exhibiting branching and anastomosis during tumor-induced angiogenesis. *Biophys. J.*, *92*, 3105–3121.

Bentley, K., Gerhardt, H., & Bates, P. A. (2008). Agent-based simulation of notch-mediated tip cell selection in angiogenic sprout initialisation. *J. Theor. Biol.*, *250*(1), 25–36.

Brooker, R., Hozumi, K., & Lewis, J. (2006). Notch ligands with contrasting functions: jagged1 and delta1 in the mouse inner ear. *Development*, *133*, 1277–1286.

Byrne, H. M., & Chaplain, M. A. J. (1995). Mathematical models for tumour angiogenesis: numerical simulations and nonlinear wave solutions. *Bull. Math. Biol.*, *57*, 461–486.

Cai, Y., Shixiong, X., Wu, J., & Long, Q. (2011). Coupled modelling of tumour angiogenesis, tumour growth and blood perfusion. *J. Theor. Biol.*, *279*, 90–101.

Carmeliet, P., & Jain, R. K. (2011). Principles and mechanisms of vessel normalization for cancer and other angiogenic diseases. *Nat. Rev., Drug Discov.*, *10*, 417–427.

Carr, R. T., & Wickham, L. L. (1991). Influence of vessel diameter on red cell distribution at microvascular bifurcations. *Microvasc. Res.*, *41*, 184–196.

Chaplain, M. A. J. (2000). Mathematical modelling of angiogenesis. *J. Neurooncol.*, *50*, 37–51.

Chaplain, M. A. J., & Stuart, A. M. (1993). A model mechanism for the chemotactic response of endothelial cells to tumour angiogenesis factor. *IMA J. Math. Appl. Med. Biol.*, *10*, 149–168.

Chaplain, M. A. J., McDougall, S. R., & Anderson, A. R. A. (2006). Mathematical modeling of tumour-induced angiogenesis. *Annu. Rev. Biomed. Eng.*, *8*, 233–257.

Claxton, S., & Fruttiger, M. (2003). Role of arteries in oxygen induced vaso-obliteration. *Exp. Eye Res.*, *77*, 305–311.

Das, A., Lauffenburger, D., Asada, H., & Kamm, R. D. (2010). A hybrid continuum-discrete modelling approach to predict and control angiogenesis: analysis of combinatorial growth factor and matrix effects on vessel-sprouting morphology. *Philos. Trans. R. Soc. A*, *368*, 2937–2960.

Davies, M. H., Stempel, A. J., Hubert, K. E., & Powers, M. R. (2010). Altered vascular expression of EphrinB2 and EphB4 in a model of oxygen-induced retinopathy. *Dev. Dyn.*, *239*, 1695–1707.

Dorrell, M. I., Aguilar, E., & Friedlander, M. (2002). Retinal vascular development is mediated by endothelial filopodia, a preexisting astrocytic template and specific R-cadherin adhesion. *Investig. Ophthalmol. Vis. Sci.*, *43*(11), 3500–3510.

Dorrell, M. I., Aguilar, E., Jacobson, R., Trauger, S. A., Friedlander, J., Siuzdak, G., & Friedlander, M. (2010). Maintaining retinal astrocytes normalizes revascularization and prevents vascular pathology associated with oxygen-induced retinopathy. *GLIA*, *58*, 43–54.

Enden, G., & Popel, A. S. (1994). A numerical study of plasma skimming in small vascular bifurcations. *J. Biomech. Eng.*, *119*, 79–88.

Erber, R., Eichelsbacher, U., Powajbo, V., Korn, T., Djonov, V., Lin, J., Hammes, H. P., Grobholz, R., Ullrich, A., & Vajkoczy, P. (2006). EphB4 controls blood vascular morphogenesis during postnatal angiogenesis. *EMBO J.*, *25*, 628–641.

Fenton, B. M., Carr, R. T., & Cokelet, G. R. (1985). Nonuniform red cell distribution in 20–100 micron bifurcations. *Microvasc. Res.*, *29*, 103–126.

Ferrara, N., Houck, K., Jakeman, L., & Leung, D. W. (1992). Molecular and biological properties of the vascular endothelial growth factor family of proteins. *Endocr. Rev.*, *13*, 18–32.

Ferrara, N., Mass, R. D., Campa, C., & Kim, R. (2007). Targeting VEGF-A to treat cancer and age-related macular degeneration. *Annu. Rev. Med.*, *58*, 491–504.

Flegg, J. A., McElwain, D. L. S., Byrne, H. M., & Turner, I. W. (2009). A three species model to simulate application of hyperbaric oxygen therapy to chronic wounds. *PLoS Comput. Biol.*, *5*, e1000451.

Folkman, J. (1995). Angiogenesis in cancer, vascular, rheumatoid and other disease. *Nat. Med.*, *1*(1), 27–31.

Fruttiger, M. (2002). Development of the mouse retinal vasculature: angiogenesis versus vasculogenesis. *Investig. Ophthalmol. Vis. Sci.*, *43*, 522–527.

Fruttiger, M., Calver, A. R., Kruger, W. H., Mudhar, H. S., Michalovich, D., Takakura, N., Nishikawa, S., & Richardson, W. D. (1996). PDGF mediates a neuron-astrocyte interaction in the developing retina. *Neuron*, *17*(6), 1117–1131.

Ganesan, P., He, S., & Xu, H. (2010). Analysis of retinal circulation using an image-based network model of retinal vasculature. *Microvasc. Res.*, *80*, 99–109.

Gariano, R. F. (2003). Cellular mechanisms in retinal vascular development. *Prog. Retin. Eye Res.*, *22*(3), 295–306.

Gerhardt, H. (2008). VEGF and endothelial guidance in angiogenic sprouting. *Organogenesis*, *4*(4), 241–246.

Gerhardt, H., Golding, M., Fruttiger, M., Ruhrberg, C., Lundkvist, A., Abramsson, A., Jeltsch, M., Mitchell, C., Alitalo, K., Shima, D., & Betsholtz, C. (2003). VEGF guides angiogenic sprouting utilizing endothelial tip cell filopodia. *J. Cell Biol.*, *161*(6), 1163–1177.

He, S., Prasanna, G., & Yorio, T. (2007). Endothelin-1-mediated signaling in the expression of matrix metalloproteinases and tissue inhibitors of metalloproteinases in astrocytes. *Investig. Ophthalmol. Vis. Sci.*, *48*, 3737–3745.

Jackson, T., & Zheng, X. (2010). A cell-based model of endothelial cell migration, proliferation and maturation during corneal angiogenesis. *Bull. Math. Biol.*, *72*, 830–868.

Karagiannis, E. D., & Popel, A. S. (2006). Distinct modes of collagen type I proteolysis by matrix metalloproteinase (MMP) 2 and membrane type I MMP during the migration of a tip endothelial cell: insights from a computational model. *J. Theor. Biol.*, *238*, 124–145.

Keyt, B. A., Berleau, L. T., Nguyen, H. V., Chen, H., Heinsohn, H., Vandlen, R., & Ferrara, N. (1996). The carboxyl-terminal domain (111-165) of vascular endothelial growth factor is critical for its mitogenic potency. *J. Biol. Chem.*, *271*, 7788–7795.

Klitzman, B., & Johnson, P. C. (1982). Capillary network geometry and red cell distribution in hamster cremaster muscle. *Am. J. Physiol.*, *242*, 211–219.

Levick, J. R. (2000). *An introduction to cardiovascular physiology* (3rd ed.). London: Arnold.

Levine, H. A., Pamuk, S., Sleeman, B. D., & Nielsen-Hamilton, M. (2001). Mathematical modeling of the capillary formation and development in tumor angiogenesis: penetration into the stroma. *Bull. Math. Biol.*, *63*(5), 801–863.

Liu, D., Wood, N. B., Witt, N., Hughes, A. D., Thom, S. A., & Xu, X. Y. (2009). Computational analysis of oxygen transport in the retinal arterial network. *Curr. Eye Res.*, *34*(11), 945–956.

Machado, M. J. C., Watson, M. G., Devlin, A. H., Chaplain, M. A. J., McDougall, S. R., & Mitchell, C. A. (2010). Dynamics of angiogenesis during wound healing: a coupled in vivo and in silico study. *Microcirculation*, *18*, 183–197.

Macklin, P., McDougall, S., Anderson, A. R. A., Chaplain, M. A. J., Cristini, V., & Lowengrub, J. (2009). Multiscale modelling and nonlinear simulation of vascular tumour growth. *J. Math. Biol.*, *58*, 765–798.

Maggelakis, S. A., & Savakis, A. E. (1996). A mathematical model of growth factor induced capillary growth in the retina. *Math. Comput. Model.*, *24*, 33–41.

Maggelakis, S. A., & Savakis, A. E. (1999). A mathematical model of retinal neovascularization. *Math. Comput. Model.*, *29*, 91–97.

Mantzaris, N. V., Webb, S., & Othmer, H. G. (2004). Mathematical modeling of tumor-induced angiogenesis. *J. Math. Biol.*, *49*, 111–187.

McDougall, S. R., Anderson, A. R. A., Chaplain, M. A. J., & Sherratt, J. A. (2002). Mathematical modelling of flow through vascular networks: implications for tumour-induced angiogenesis and chemotherapy strategies. *Bull. Math. Biol.*, *64*, 673–702.

McDougall, S. R., Anderson, A. R. A., & Chaplain, M. A. J. (2006). Mathematical modelling of dynamic adaptive tumour-induced angiogenesis: clinical implications and therapeutic targeting strategies. *J. Theor. Biol.*, *241*, 564–589.

Mitchell, A. R., & Griffiths, D. F. (1980). *The finite difference method in partial differential equations*. Chichester: Wiley.

Mitchell, C. A., Rutland, C. S., Walker, M., Nasir, M., Foss, A. J., Stewart, C., Gerhardt, H., Konerding, M. A., Risau, W., & Drexler, H. C. (2006). Unique vascular phenotypes following over-expression of individual VEGFA isoforms from the developing lens. *Angiogenesis*, *9*(4), 209–224.

Mudhar, H. S., Pollock, R. A., Wang, C., Stiles, C. D., & Richardson, W. D. (1993). PDGF and its receptors in the developing rodent retina and optic nerve. *Development*, *118*(2), 539–552.

Ng, Y. S., Rohan, R., Sunday, M. E., Demello, D. E., & D'Amore, P. A. (2001). Differential expression of VEGF isoforms in mouse during development and in the adult. *Dev. Dyn.*, *220*, 112–121.

Olsen, L., Sherratt, J. A., Maini, P. K., & Arnold, F. (1997). A mathematical model for the capillary endothelial cell-extracellular matrix interactions in wound-healing angiogenesis. *IMA J. Math. Appl. Med. Biol.*, *14*, 261–281.

Orme, M. E., & Chaplain, M. A. J. (1997). Two-dimensional models of tumour angiogenesis and anti-angiogenesis strategies. *IMA J. Math. Appl. Med. Biol.*, *14*, 189–205.

Owen, M. R., Alarcon, T., & Maini, P. K. (2009a). Angiogenesis and vascular remodelling in normal and cancerous tissues. *J. Math. Biol.*, *58*, 689–721.

Owen, M. R., Alarcon, T., Maini, P. K., & Byrne, H. M. (2009b). Angiogenesis and vascular remodelling in normal and cancerous tissues. *J. Math. Biol.*, *58*, 689–721.

Park, J. E., Keller, G. A., & Ferrara, N. (1993). The vascular endothelial growth factor (VEGF) isoforms: differential deposition into the subepithelial extracellular matrix and bioactivity of extracellular matrix-bound VEGF. *Mol. Biol. Cell*, *4*, 1317–1326.

Peirce, S. M. (2008). Computational and mathematical modelling of angiogenesis. *Microcirculation*, *15*(8), 739–751.

Perfahl, H., Byrne, H. M., Chen, T., Estrella, V., Lapin, A., Gatenby, R. A., Gillies, R. J., Lloyd, M. C., Maini, P. K., Reuss, M., & Owen, M. R. (2011). Multiscale modelling of vascular tumour growth in 3D: the roles of domain size and boundary conditions. *PloS One*, *6*(4), e14790.

Pettet, G. J., Byrne, H. M., McElwain, D. L. S., & Norbury, J. (1996). A model of wound-healing angiogenesis in soft tissue. *Math. Biosci.*, *136*, 35–63.

Plank, M. J., & Sleeman, B. D. (2004). Lattice and non-lattice models of tumour angiogenesis. *Bull. Math. Biol.*, *66*, 1785–1819.

Pons-Salort, M., van der Sanden, B., Juhem, A., Popov, A., & Stephanou, A. (2012). A computational framework to assess the efficacy of cytotoxic molecules and vascular disrupting agents against solid tumours. *Math. Model. Nat. Phenom.*, *7*, 49–77.

Pries, A. R., Ley, K., Claassen, M., & Gaehtgens, P. (1989). Red cell distribution at microvascular bifurcations. *Microvasc. Res.*, *38*, 81–101.

Pries, A. R., Fritzsche, A., Ley, K., & Gaehtgens, P. (1992). Redistribution of red blood cell flow in microcirculatory networks by hemodilution. *Circ. Res.*, *70*, 1113–1121.

Pries, A. R., Secomb, T. W., Gessner, T., Sperandio, M. B., Gross, J. F., & Gaehtgens, P. (1994). Resistance to blood flow in microvessels in vivo. *Circ. Res.*, *75*, 904–915.

Pries, A. R., Secomb, T. W., & Gaehtgens, P. (1998). Structural adaptation and stability of microvascular networks: theory and simulations. *Am. J. Physiol.*, *275*, 349–360.

Pries, A. R., Reglin, B., & Secomb, T. W. (2001). Structural adaptation of microvascular networks: functional roles of adaptive responses. *Am. J. Physiol., Heart Circ. Physiol.*, *281*, 1015–1025.

Pries, A. R., Hopfner, M., le Noble, F., Dewhirst, M. W., & Secomb, T. W. (2010). The shunt problem: control of functional shunting in normal and tumour vasculature. *Nat. Rev. Cancer*, *10*, 587–593.

Rutland, C. S., Mitchell, C. A., Nasir, M., Konerding, M. A., & Drexler, H. C. (2007). Microphthalmia, persistent hyperplastic hyaloid vasculature and lens anomalies following overexpression of VEGF-A188 from the alphaA-crystallin promoter. *Mol. Vis.*, *13*, 47–56.

Sainson, R. C. A., & Harris, A. L. (2006). Hypoxia-regulated differentiation: let's step it up a Notch. *Trends Mol. Med.*, *12*(4), 141–143.

Sainson, R., Aoto, J., Nakatsu, M. N., Holderfield, M., Conn, E., Koller, E., & Hughes, C. C. W. (2005). Cell-autonomous Notch signalling regulates endothelial cell branching and proliferation during vascular tubulogenesis. *FASEB J.*, *19*(8), 1027–1029.

Schmid-Schoenbein, G. W., Skalak, R., Usami, S., & Chien, S. (1980). Cell distribution in capillary networks. *Microvasc. Res.*, *19*, 18–44.

Schugart, R. C., Friedman, A., Zhao, R., & Sen, C. K. (2008). Wound angiogenesis as a function of tissue oxygen tension: a mathematical model. *Proc. Natl. Acad. Sci.*, *105*, 2628–2633.

Scott, A., Powner, M. B., Gandhi, P., Clarkin, C., Gutmann, D. H., Johnson, R. S., Ferrara, N., & Fruttiger, M. (2010). Astrocyte-derived vascular endothelial growth factor stabilizes vessels in the developing retinal vasculature. *PLoS One*, *5*, e11863.

Secomb, T. W., Alberding, J. P., Hsu, R., & Pries, A. R. (2007). Simulation of angiogenesis, remodeling and pruning in microvascular networks. *FASEB J.*, *21*, 897.10.

Shima, D. T., Kuroki, M., Deutsch, U., Ng, Y. S., Adamis, A. P., & D'Amore, P. A. (1996). The mouse gene for vascular endothelial growth factor. Genomic structure, definition of the transcriptional unit, and characterization of transcriptional and post-transcriptional regulatory sequences. *J. Biol. Chem.*, *271*, 3877–3883.

Shirinifard, A., Gens, J. S., Zaiden, B. L., Poplawski, N. J., Swat, M., & Glazier, J. A. (2009). 3D multi-cell simulation of tumour growth and angiogenesis. *PloS One*, *4*(10), e7190.

Stalmans, I., Ng, Y. S., Rohan, R., Fruttiger, M., Bouche, A., Yuce, A., Fujisawa, H., Hermans, B., Shani, M., Jansen, S., Hicklin, D., Anderson, D. J., Gardiner, T., Hammes, H. P., Moons, L., Dewerchin, M., Collen, D., Carmeliet, P., & D'Amore, P. A. (2002). Arteriolar and venular patterning in retinas of mice selectively expressing VEGF isoforms. *J. Clin. Invest.*, *109*, 327–336.

Stephanou, A., McDougall, S. R., Anderson, A. R. A., & Chaplain, M. A. J. (2005). Mathematical modelling of flow in 2D and 3D vascular networks: applications to anti-angiogenic and chemotherapeutic drug strategies. *Math. Comput. Model.*, *41*, 1137–1156.

Stephanou, A., McDougall, S. R., Anderson, A. R. A., & Chaplain, M. A. J. (2006). Mathematical modelling of the influence of blood rheological properties upon adaptative tumour-induced angiogenesis. *Math. Comput. Model.*, *44*, 96–123.

Stokes, C. L., & Lauffenburger, D. A. (1991). Analysis of the roles of microvessel endothelial cell random motility and chemotaxis in angiogenesis. *J. Theor. Biol. 152*, 377–403.

Stone, J., Chan-Ling, T., Pe'er, J., Itin, A., Gnessin, H., & Keshet, E. (1996). Roles of vascular endothelial growth factor and astrocyte degeneration in the genesis of retinopathy of prematurity. *Investig. Ophthalmol. Vis. Sci.*, *37*, 290–299.

Stout, A. U., & Stout, J. T. (2003). Retinopathy of prematurity. *Pediatr. Clin. North Am.*, *50*, 77–87.

Szczerba, D., & Szekely, G. (2005). Computational model of flow-tissue interactions in intussusceptive angiogenesis. *J. Theor. Biol.*, *234*, 87–97.

Szczerba, D., Kurz, H., & Szekely, G. (2009). A computational model of intussusceptive microvascular growth and remodelling. *J. Theor. Biol.*, *261*, 570–583.

Uemura, A., Kusuhara, S., Wiegand, S. J., Yu, R. T., & Nishikawa, S. (2006). Tlx acts as a proangiogenic switch by regulating extracellular assembly of fibronectin matrices in retinal astrocytes. *J. Clin. Invest.*, *116*(2), 369–377.

Weidemann, A., Krohne, T. U., Aguilar, E., Kurihara, T., Takeda, N., Dorrell, M. I., Simon, M. C., Haase, V. H., Friedlander, M., & Johnson, R. S., (2010). Astrocyte hypoxic response is essential for pathological but not developmental angiogenesis of the retina. *GLIA*, *58*(10), 1177–1185.

Welter, M., Bartha, K., & Rieger, H. (2008). Emergent vascular network inhomogeneities and resulting blood flow patterns in a growing tumor. *J. Theor. Biol.*, *250*, 257–280.

Welter, M., Bartha, K., & Rieger, H. (2009). Vascular remodelling of an arterio-venous blood vessel network during solid tumour growth. *J. Theor. Biol.*, *259*, 405–422.

West, H., Richardson, W. D., & Fruttiger, M. (2005). Stabilization of the retinal vascular network by reciprocal feedback between blood vessels and astrocytes. *Development*, *132*(8), 1855–1862.

Williams, C. K., Li, J. L., Murga, M., Harris, A. L., & Tosato, G. (2006). Up-regulation of the Notch ligand delta-like 4 inhibits VEGF induced endothelial cell function. *Blood*, *107*(3), 931–939.

Wu, J., Xu, S., Long, Q., Collins, M. W., König, C., Zhao, G., Jiang, Y., & Padhani, A. R. (2008). Coupled modeling of blood perfusion in intravascular, interstitial spaces in tumor microvasculature. *J. Biomech.*, *41*, 996–1004.

Wu, J., Long, Q., Xu, S., & Padhani, A. R. (2009). Study of tumor blood perfusion and its variation due to vascular normalization by anti-angiogenic therapy based on 3D angiogenic microvasculature. *J. Biomech.*, *42*, 712–721.

Xue, C., Friedman, A., & Sen, C. K. (2009). A mathematical model of ischemic cutaneous wounds. *Proc. Natl. Acad. Sci.*, *106*, 16782–16787.

Yana, I., Sagara, H., Takaki, S., Takatsu, K., Nakamura, K., Nakao, K., Katsuki, M., Taniguchi, S., Aoki, T., Sato, H., Weiss, S. J., & Seiki, M. (2007). Crosstalk between neovessels and mural cells directs the site-specific expression of MT1-MMP to endothelial tip cells. *J. Cell Sci.*, *120*, 1607–1614.

Yen, R. T., & Fung, Y. C. (1978). Effect of velocity distribution on red cell distribution in capillary blood vessels. *Am. J. Physiol.*, *235*, 251–257.

Zhang, M., Cheng, X., & Chintala, S. K. (2004). Optic nerve ligation leads to astrocyte-associated matrix metalloproteinase-9 induction in the mouse retina. *Neurosci. Lett.*, *356*, 140–144.

Zheng, X., Wise, S. M., & Cristini, V. (2005). Nonlinear simulation of tumor necrosis, neo-vascularization and tissue invasion via an adaptive finite-element/level-set method. *Bull. Math. Biol.*, *67*, 211–259.